UNIVERSITY OF ZULULAND

SYNTHESIS AND CHARACTERIZATION OF TUNGSTEN OXIDE WO_3 NANOSTRUCTURES THIN FILMS FOR GAS SENSING APPLICATIONS

Dissertation submitted in fulfilment of the requirements for the degree of Master of Science to the:

Faculty of Science and Agriculture

Department of Physics and Engineering

UNIVERSITY OF ZULULAND

Supervisors: Dr C.L. Ndlangamandla

Dr T.P. Jili

Co-Supervisor: Prof. O.M. Ndwandwe

Submitted by

Thokozani Mpanza (201234905)

February 2018

DECLARATION

I, the undersigned, hereby declare that the work contained in this dissertation is my own original work and that I have not previously in its entirety or in part submitted it at any university for a degree.

Signature:……..

Date:……..

ABSTRACT

This work presents the synthesis of a room temperature gas sensor based on tungsten oxide (WO_3) thin films. The synthesis of WO_3 thin films was carried out using a direct current (DC) reactive magnetron sputtering at different deposition temperatures (300, 400 and 500 ºC). The deposition time, pressure, power, oxygen and argon flow rates were kept constant. The purpose of this work was to investigate the effect of deposition temperature on WO_3 based sensor film and to see if the deposition temperature can be optimised in order to improve the gas sensing properties of WO_3 thin films. The scanning electron microscope (SEM) equipped with energy dispersive x-ray spectroscopy (EDS) was utilized to study the surface morphology and chemical composition or stoichiometry of all samples. The results from the SEM images showed that as the deposition temperature changes, the morphology of WO_3 film also changes. X-ray diffraction (XRD) was then used to study the crystal structure of the samples and the samples were found to be amorphous at 300 ºC and polycrystalline at 400 ºC and 500 ºC. It was also observed from XRD that the change in deposition temperature resulted in the formation of different phases and orientations in WO_3 films since WO_3 film deposited at 300 ºC found to be amorphous, at 400 ºC it was hexagonal in crystal structure, and WO_3 film deposited at 500 ºC was found to be tetragonal. When using Scherre's equation it was found that as the temperature increases, the grain size of the samples also increases. The atomic force microscopy (AFM) was then used to study the roughness of the samples. The AFM revealed that as the deposition temperature increases the roughness of the samples also increases. Rutherford backscattering spectrometry (RBS) was used to study the composition and thickness of the samples. RBS confirmed that the samples deposited were WO_3. It was found that as the deposition temperature increases the thickness of the thin films also increases. The gas sensing properties of the samples were investigated using the gas sensor apparatus (Kenosistec) at room temperature and it was found that increasing the deposition temperature from 300 ºC to 500 ºC enhanced the gas sensing properties of the samples.

ACKNOWLEDGEMENTS

I would like to extend my gratitude to the following who contributed to the success of this project:

God who have kept me alive, giving me strength and courage through all difficulties and challenges.

Prof O.M. Ndwandwe, Dr C.L. Ndlangamandla and Dr T.P. Jili for designing this project and for being good supervisors by always being there for me whenever I need assistance.

Mr C.T. Thethwayo and Mr A.P. Sefage for introducing me to the use of the sputtering system and for their guidance and kindness whenever I need help.

Mr C.T. Thethwayo for his good assistance during the SEM and EDS work.

Dr S Mlowe and Sphamandla for their assistance during the XRD and AFM work.

Dr Morgan Madhuku for his good assistance during the RBS work.

Dr S Nkosi for his good assistance during the gas sensing work.

All my family members for being supportive and always encouraging me whenever I loses hope.

The University of Zululand, Physics and Engineering staff and MSc student Mr N.W. Khoza for their support and motivation.

Mrs N.C. Mothapo for being supportive and kind whenever I needed assistance with printing.

NRF/DST, iThemba LABS and the research committee of the University of Zululand for financial support during this research work.

DEDICATION

Dedicated to my parents, Mrs Khangezile and Mr Mbongeni Mhlomiseni Mpanza

TABLE OF CONTENTS

LIST OF FIGURES

LIST OF TABLES

CHAPTER 1

1. INTRODUCTION

1.1. Nanotechnology

Nanoscience is a study of the fundamental principles of molecules and structures with nanoscale size (between 1 nm and 100 nm). Nanotechnology is the application of nanoscience in technological devices and also the manipulation of materials in nanoscale. Manipulation at the nanoscale changes the physical, chemical and biological properties of materials in ways different from what would occur at micro or bulk level **[1,2]**. Nanoscale is where quantum effects rule the behaviour and properties of material particles **[2]**. In this scale range the properties of materials are dependent on the size of their microstructure. Some examples of such properties are optical, geometrical, magnetic permeability, electrical conductivity, chemical reactivity and catalytic properties **[2**,**3]**.

In this study, nanotechnology was used to design one of the technological devices called a gas sensor. The increase in exhaust emissions of gases from industries has put a large demand on the sensitive and selective detection of hazardous gases for environmental pollution monitoring, process control and safety for human health **[3,4,5]**. This has contributed to the fabrication of gas sensor devices **[3,4,5,6,7]**. In this study, we aimed to synthesize thin films of WO_3 nanostructures for gas sensing applications by using the direct current (DC) magnetron sputtering method. The gas sensing properties of WO_3 thin films, such as gas response, sensitivity, selectivity, response time, recovery time and repeatability towards gases in different concentrations were investigated using the gas sensor test apparatus (Kenosistec (model: KSGAS6S), manufactured by Angelantoni

industries in Italy). The work was done at the University of Zululand in the Department of Physics and Engineering.

1.2. Problem identification

The increase in production or emission of gases from industries has a very bad impact on the environment. Some of those gases are not environmentally friendly since they are toxic or poisonous. Such gases cause air pollution, acid rain, and have a bad impact on crops we grow. Some of these gases are also dangerous to humans and animals since they can cause illnesses. Therefore, gas sensing devices are important for resolving these issues. A gas sensing device detects and absorbs gases and in this study a gas sensor was fabricated. This gas sensor was expected to detect and absorb even small concentrations of gases. Some of the gases are harmful even at small concentrations **[3,4,5,6,7,8,9]**.

It is therefore important to have gas sensors for detecting such toxic gases, and to have new ways of engineering or fabricating gas sensors and to improve their sensitivity and selectivity. Semiconducting metal oxides have been reported to be the most promising materials for gas sensing **[3-9]**. It is important to find suitable nanostructures for these materials to improve their gas sensing properties **[6,7]**. Recent studies have shown good gas sensing properties at temperatures between 200 ^{o}C to 500 ^{o}C for various gas sensors, including gas sensors based on WO_3 nanostructures. However, these sensors do not sense well at room temperatures. WO_3 gas sensors require high operating temperatures while sensing. This is because of its high activation energy for reacting with gas molecules or for chemisorption to occur **[3,10]**. However, environment that people normally work in when they are at their work stations is room temperature. Therefore, it is very important to have a good performing gas sensor not only at high

temperature but also at room temperatures. It has been reported in the literature that gas responses of gas sensors decrease with the decrease of the concentration of the analyte gas **[3-9]**.

1.3. Aims of the study

- Development of a gas sensor based on WO3 nanostructured thin films with the capability to sense at room temperature.

1.4. Objectives of the study

- To synthesize thin films of WO_3 nanostructures on glass, silicon and alumina substrates using DC magnetron sputtering technique on evacuated environment at different deposition temperatures.
- To characterize sputter deposited thin films of WO_3 nanostructures using various analytical techniques, such as X-ray diffraction (XRD), scanning electron microscopy (SEM) equipped with energy dispersive spectroscopy (EDS), atomic force microscopy (AFM) and Rutherford backscattering spectroscopy (RBS).
- To test gas sensing properties (gas response: sensitivity, selectivity, response time, recovery time) of WO_3 nanostructures for various target gases at different concentrations (ppm) at room temperature, using the gas sensor test apparatus (Kenosistec).
- To investigate the effect of annealing temperatures (temperatures used during deposition) on gas sensing properties of WO_3.

1.5. Thesis outline

In this study the DC magnetron sputtering method is used because of its ability to produce good uniform thin films which are good for gas sensing. This apparatus is available at The University of Zululand.

The thesis is organized as follow:

- Chapter one gives an introduction to nanotechnology and to its importance in technological devices.
- Chapter two gives a literature review on WO_3 metal oxide semiconductors.
- Chapter three describes different types of deposition and characterization techniques.
- Chapter four describes the synthesis and characterization of thin films of WO_3 nanostructures.
- Chapter five discusses the gas sensing properties of WO_3 thin films.
- Chapter six gives a summary and conclusion.

CHAPTER 2:

2. LITERATURE REVIEW

2.1. Recent progress on WO_3 and its applications

Metal oxide nanoparticles have attracted considerable interest in recent years due to their unique physical and chemical properties in nanoscale. These properties differ significantly from the bulk or molecular properties of the respective materials **[4]**. Tungsten oxide (WO_3) is an n-type metal oxide semiconducting material with a band gap of about 2.7 eV **[5]**. WO_3 is considered to be a highly promising material for a broad range of applications such as in electronic devices, super-capacitors, optical systems, gas sensors, solar energy, photocatalysts and biosensors **[6,7,8,9,11,12,13]**. This is because of its unique structural and physical properties, non-toxicity, and high chemical stability **[6,7,8,9,11]**. WO_3 exhibit various phases at varying temperature for example, it is tetragonal at temperatures above 740 ºC, orthorhombic in the region 330 ºC to 740 ºC, monoclinic in the range of 17 ºC to 330 ºC and triclinic between -50 ºC and 17 ºC **[7,8,9,11,12]**. The most common structure of WO_3 is monoclinic **[7]**.

Some previous studies have reported that n-type metal oxide nanostructures are promising materials for gas sensing since they have good electrical properties, excellent stability in various environments and are suitable for doping **[8-11]**. Chemical gas sensors based on WO_3 nanostructures have drawn considerable attention of researchers due to their high responses, good sensitivity and selectivity in detecting a range of gases in the parts per million (ppm) scale **[11-12]**. WO_3 has been reported to be sensitive to a broad range of both oxidizing and reducing gases such as NO_2, NH_3, CO, O_3, C_2H_6O, H_2, H_2S, SO_2 and NO **[4,6,11,13]**. Some of these gases are dangerous at high ppm concentrations, like sulphur dioxide (SO_2), hydrogen sulphide (H_2S) and

nitrogen dioxide NO_2 **[4,13]**. Increase in SO_2 emission from industries when burning coal fossil fuel for energy results in air pollution and contribute to acid rain which is dangerous to human health, hence the importance of a SO_2 sensor **[13]**. NO_2 is a potentially toxic gas that can cause respiratory symptoms in humans and also contribute to the formation of acid rain **[4].** Therefore gas sensors for monitoring such toxic gases are very important.

It has been reported in recent studies that a considerable effort to improve the gas sensing properties of metal oxides gas sensors went into the use of various dopants. WO_3 gas sensors have been previously doped with Pd, Pt, Au, Cr and Ni nanoparticles and improved gas sensing properties were reported **[11-12,14]**. Hybrid materials made of semiconductor metal oxides and Carbon nanotubes (CNTs) have been studied in recent years for various applications such as photocatalysis, anode material for lithium ion batteries and gas sensing **[15,16,17]**. These studies have reported that gas sensors from hybrid materials have a better performance compared to semiconductor metal oxides and that they can detect various gases such as NH_3, NO_2, H_2, CO and liquefied petroleum gas (LPG) **[15-17]**. The CNTs-doped SnO_2 gas sensors have been reported as good gas sensors for NH_3 and NO_2 at room temperature, and have reduced the power consumption of the sensing devices in a gas sensor test apparatus **[16]**.

2.2. Characteristics of gas sensors

The characteristics or properties of gas sensors are defined by their sensor response (S). Recent studies have reported that the sensing properties of gas sensors are their sensitivity, selectivity, repeatability, response time and recovery time **[4-16,3,18,19]**. Sensitivity of the gas sensor was defined as the ability of the gas sensor to sense or detect the gas molecules when exposed to that

particular gas, whereas selectivity is the ability of the gas sensor to distinguish between different gases, being able to sense one gas with greater sensitivity in the presence of other gases **[8-15]**. Recent studies have reported that in order to check the selectivity of the gas sensor, a gas sensor is exposed to various gases **[3,18,19]**. Repeatability of the gas sensor was defined as its ability to produce or give the same sensor response when all operating and environmental conditions are kept constant over a certain period of time **[4-6]**. The response time and recovery time of the gas sensor reveal how fast the gas sensor responds to the target gas and the time it takes for the gas sensor to return to its original state (resistance) when the target gas has been released and thereafter turned off, respectively **[4-16]**.

2.3. Gas sensing mechanism

Many recent studies have defined the gas sensor response (S) to a target gas as the ratio of R_a to R_g where R_g and R_a are the electrical resistance of the sensing material (gas sensor) in the target gas and in synthetic air respectively **[3,18,19]**, as shown in the equation (2.1) below:

$$\text{sensor response } (S) = \frac{R_a}{R_g} \tag{2.1}$$

Some other studies **[8,11,20]** have defined the sensor response as in the equation (2.2) below:

$$\text{sensor response } (S) = \frac{|R_g - R_a|}{R_a} \tag{2.2}$$

It has been reported that the gas response of semiconducting metal oxide gas sensors exist only if the change in electrical resistance of a sensing material is observed when exposed to a target gas **[8-12,3,18]**. Based on previous studies **[8,3,18 ,19]**, it has been reported that the change in electrical resistance of semiconducting metal oxide based sensors is caused by the chemical adsorption and

also by the reaction of the gas molecules with the particles on the surface of the sensing material. Vacancies on the metal oxide sensing materials play a very important role on trapping the molecules of the target gas for adsorption to occur **[3,18,19]**. The reaction shown in the equation (2.3) below shows how the WO_3 gas sensor has detected NO_2 gas by its surface particles. In this reaction WO_3 electrons interact with NO_2, resulting in the formation of NO_2^- ions on the WO_3 surface **[18]**.

$$NO_2 + e^-(\text{from } WO_3) \rightarrow NO_2^-(WO_3 \text{ surface}) \quad (2.3)$$

The semiconducting gas sensing materials can be classified as p-type or n-type according to the variation of conductance when it is exposed to the oxidizing or reducing gases **[18]**. In the study of the synthesis of a cactus-like silicon nanowires/tungsten oxide nanowires NO_2 gas sensor **[3]**, WO_3 was reported to behave as an n-type semiconductor. Silicon nanowires (SiNWs) behave as a p-type semiconductor. It was reported that a SiNWs/WO_3 composite sensor showed a sudden decrease in its resistance when exposed to the oxidizing NO_2 gas, which was reported as an indication of p-type behaviour. In Figure 2.1 the structure of a SiNWs/WO_3 gas sensor is shown, and it illustrates how this sensor is adsorbing NO_2 molecules when NO_2 gas molecules come into contact with the sensor surface. The p-n hetero-interface of the SiNWs/WO_3 surface was found to provide more active adsorption sites for high adsorption of NO_2 gas to occur. The unpaired electrons on the NO_2 molecules react with the free electrons available on the surface of SiNWs dangling bonds. NO_2^- ions are formed and result in the increase of the concentration of holes in the valence band of SiNWs. The electrons are then trapped in the space charge region by diffusion,

resulting in the decrease of width in the space charge region which is also accompanied by a decrease in the resistance of the sensor exposed to the NO_2 gas **[3,18]**.

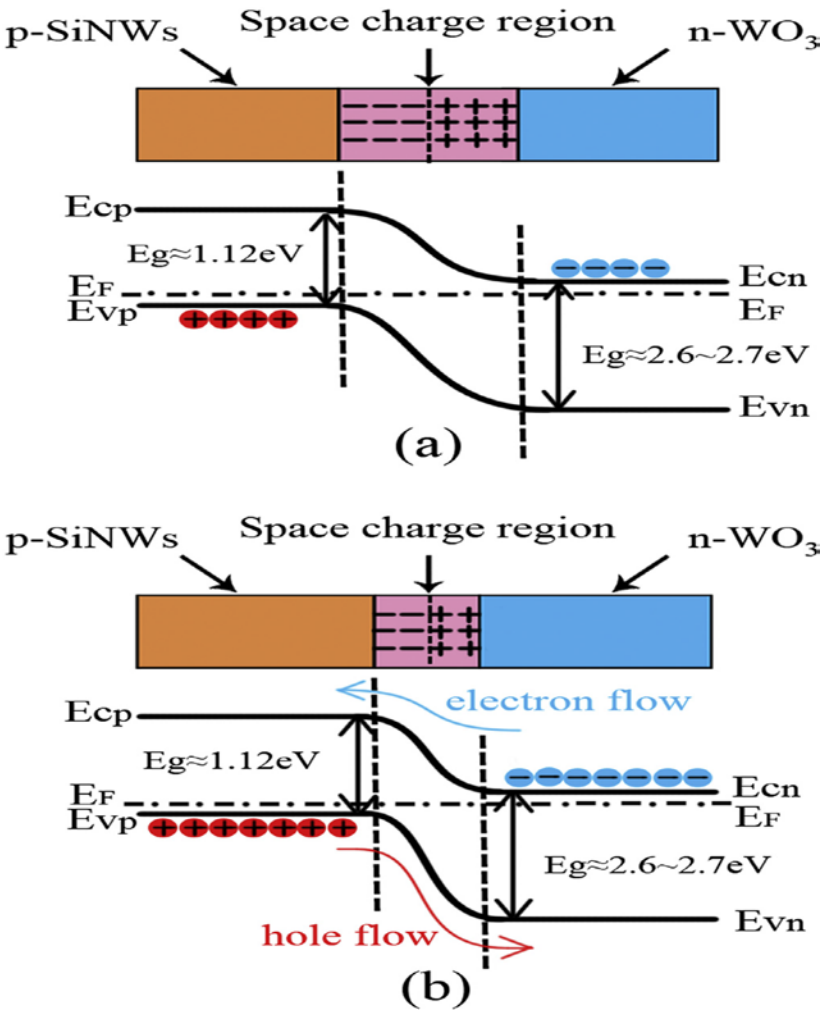

Figure 2. 1: Schematic representation of energy band diagram of (a) SiNWs/WO_3 nanowires heterojunction structure at thermal equilibrium and (b) SiNWs/WO_3 nanowires during NO_2 gas detection, where Ec is a conduction band, Ef is Fermi level, Ev is a valance band and Eg is the band gap for SiNWs WO_3 ***[3].***

Recent studies have shown that as the concentration of the target gas increases, the gas response also increases **[4-16,3,18,19]**. Figure 2.2 below shows the increase in gas response of a WO_3 gas sensor as the concentration of the target gas (NO_2) increases.

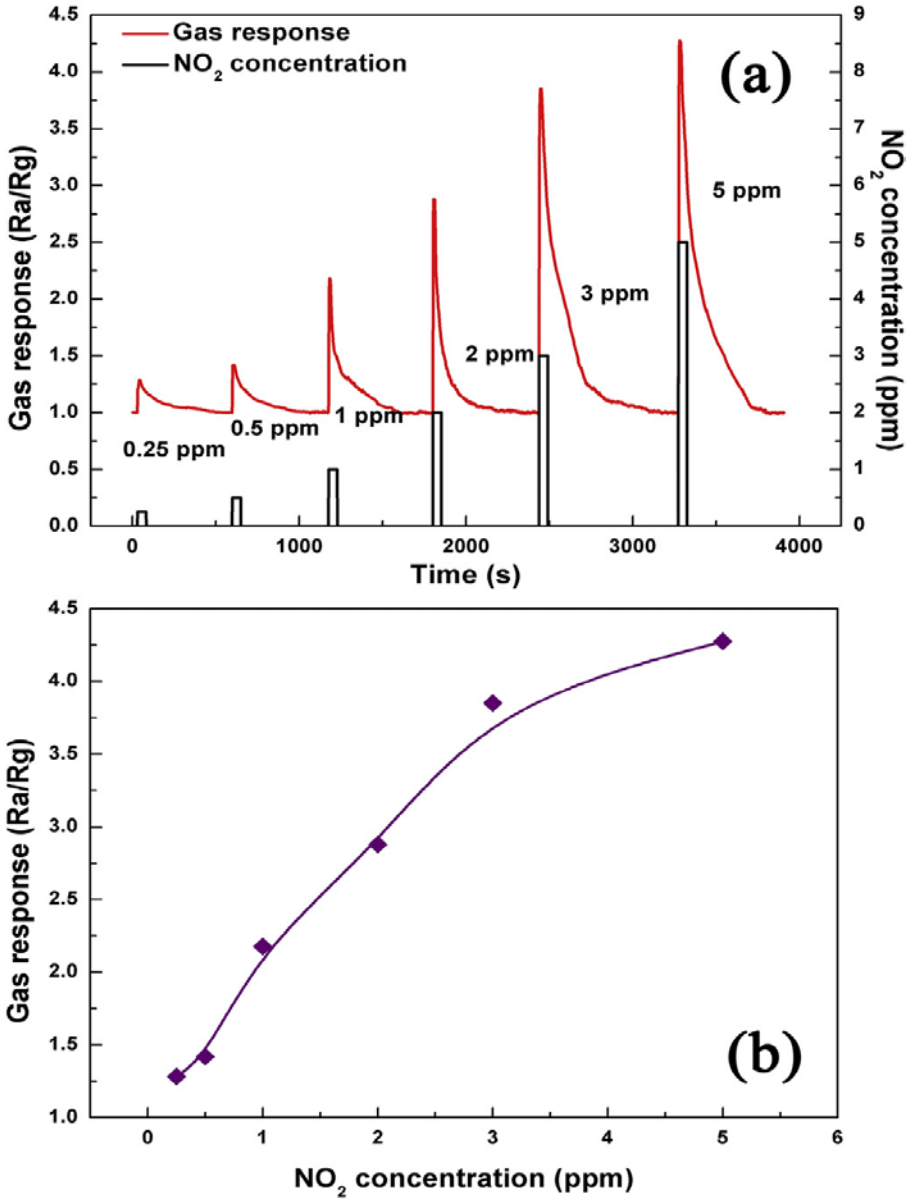

Figure 2. 2: (a) Gas sensing response curve of SiNWs/WO_3 sensor at various concentrations of NO_2 at room temperature and (b) the fitting curve of the relationship between the gas response and the concentration of NO_2 ***[3].***

Figure 2.3 shows the schematic diagram of a homemade testing system which had been used in other studies for measuring the gas sensing properties of the gas sensor material **[21]**. Various studies have used a kenosistec gas sensor testor to measure the gas sensing properties of gas sensors **[4-16]**. Figure 2.3 illustrates how the gas is introduced inside the test chamber and is sensed or detected by the sensing material inside. The digital multimeter is used to continuously measure the resistance change of the sensor and the results are observed on the data acquisition PC **[21]**.

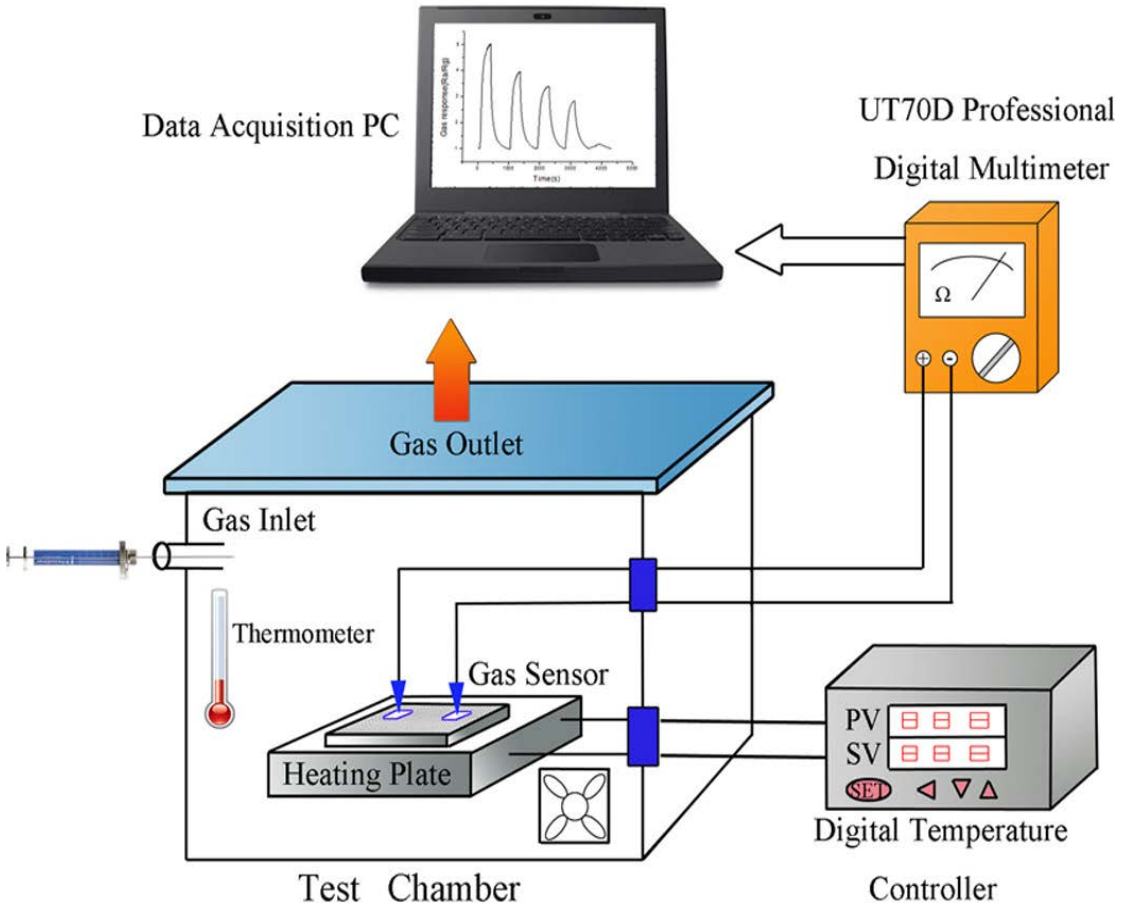

*Figure 2. 3: Schematic diagram of a gas sensor testing system **[21].***

It has been reported in various studies **[11,3,22]** that after the gas had been introduced into the testing system, the gas molecules or atoms of the target gas interact with the surface layer of the sensing material and as this interaction occurs, the resistance of the sensing material decreases quickly and saturates at a certain value until the gas is turned off. It was also reported **[6]** that the decrease in resistance of the WO_3 sensor is due to the reaction of the adsorbed oxygen atoms with the adsorbed NH_3 target gas and that free electrons are released into the sensing layer. When the NH_3 target gas is turned off and removed from the sensing layer environment through diffusion, the number of electrons in the sensing layer decreases, **[6]** causing the conductivity and the resistance of the sensing material to return to its original values **[5-7,23]**. Figure 2.4 shows the sensing response of the WO_3 sensor towards different concentrations of H_2 target gas. The WO_3 film was grown on top of a platinum (Pt) film at 500 ºC and 700 ºC and the temperature of 450 ºC was maintained during the measuring of gas sensing in the testing system ***[23]***.

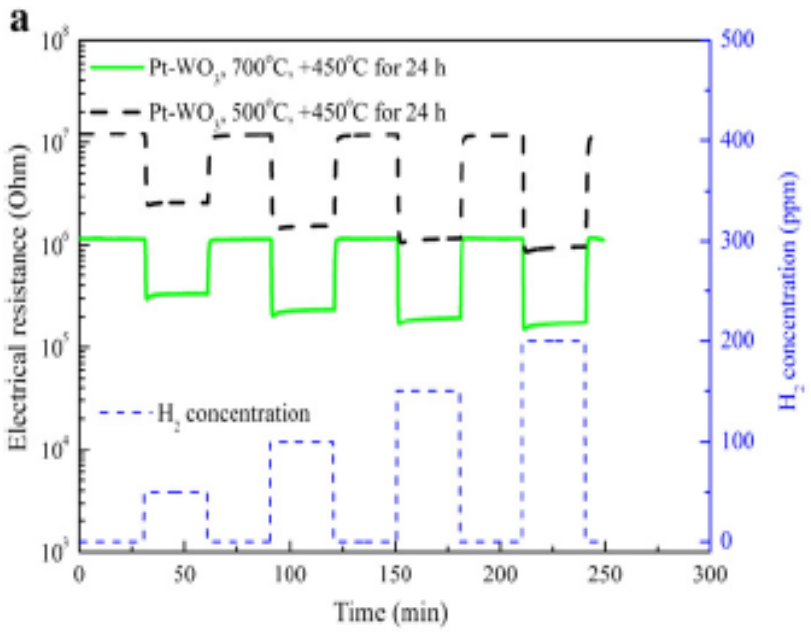

Figure 2. 4: Gas response of a WO_3 gas sensor towards different H_2 concentrations ***[23]***.

Figure 2.5 shows the WO_3 gas sensor exposed to different concentrations of different gases at 250 ºC and it can be seen that the WO_3 gas response is more favourable to acetone gas than to the other target gases. This demonstrates the selectivity property of WO_3 ***[24]***.

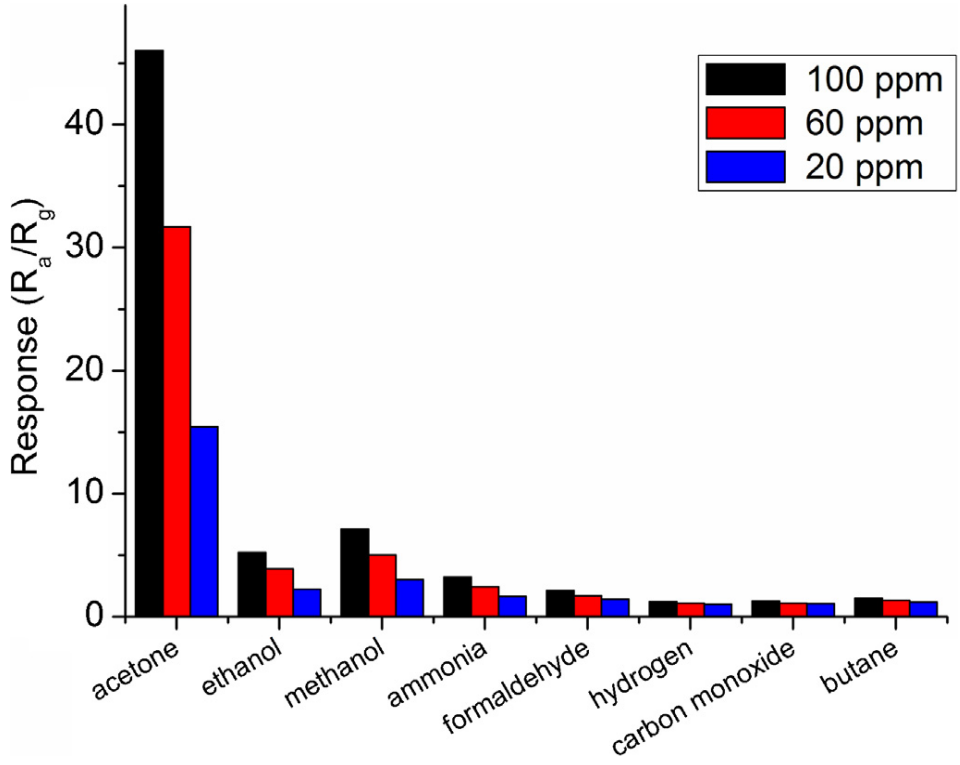

Figure 2. 5: The WO_3 sensor response towards different concentrations of different gases. WO_3 showed a selectivity property towards acetone ***[24].***

Recent studies **[21**,**22]** , have reported that the surface layer of the sensing material must have a large number of surface sites in order to enhance gas adsorption, and this is obtained if the material consists of nanostructures (e.g. nanowires, nanorods, or nanoparticles). Vacancies in the sensing surface layers increase the sensitivity and decrease the response time of the sensors towards the target gases **[22,25]**. Figure 2.6 depicts the surface morphology of WO_3 nanoparticles, which is

favourable in gas sensing. This micrograph was obtained using a scanning electron microscopy **[26]**.

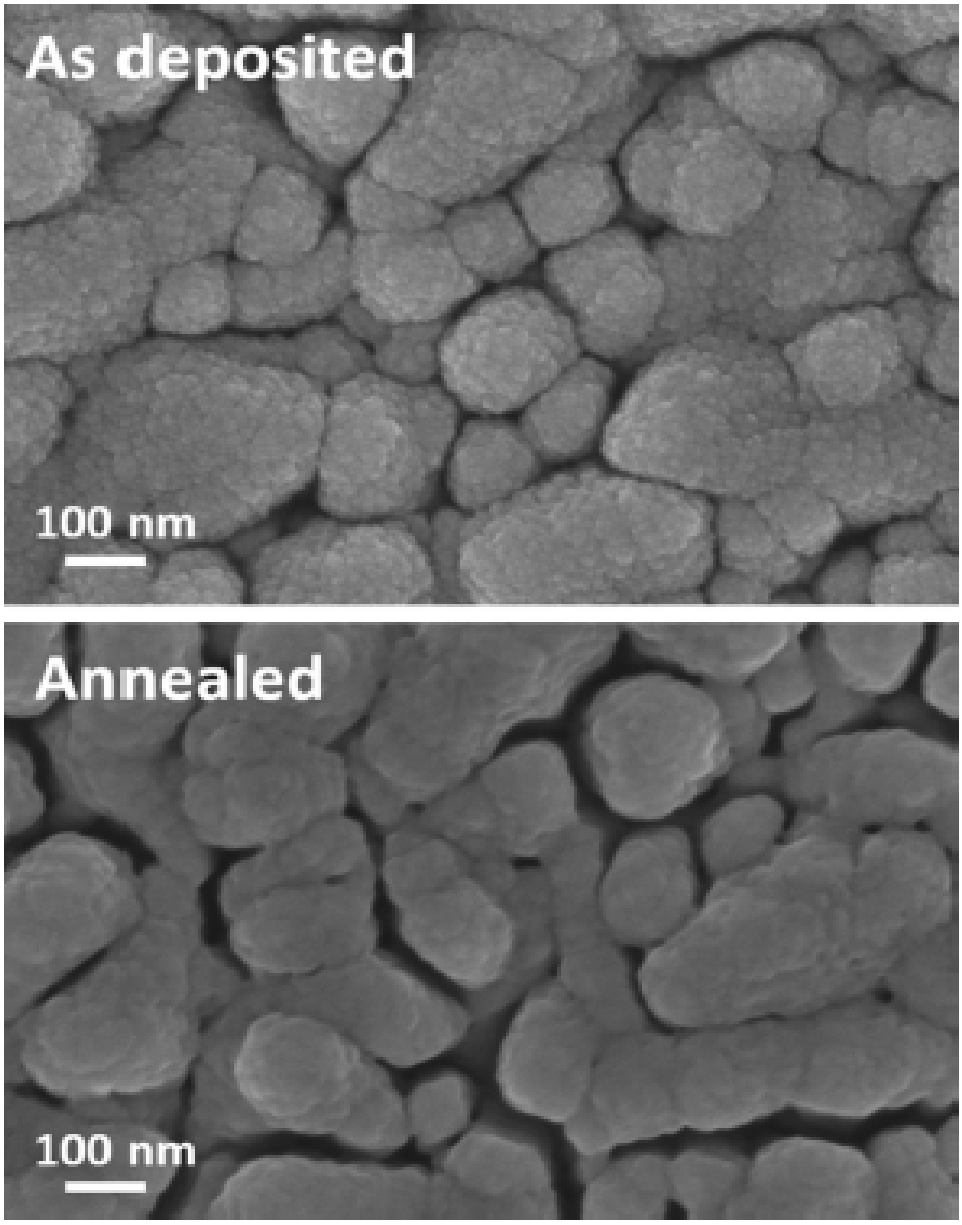

Figure 2.6: The morphology of as deposited and annealed (500 ºC) WO_3 nanoparticles determined by the SEM, as adopted from reference ***[26].***

Most previous studies on WO_3 based sensors have reported that the nanocrystalline films of WO_3 have good gas sensing properties **[11,20]**. It has been reported that the crystallites of WO_3 exhibit improved sensing performance if their dimensions are smaller (within nanoscale) **[20,22]**. Figure 2.7 shows the polycrystalline WO_3 obtained from the XRD technique. In this figure it can be seen that WO_3 was crystallized by annealing at high temperatures **[20-21]**. The polycrystalline WO_3 has diffraction peaks but amorphous WO_3 has no diffraction peaks **[20]**.

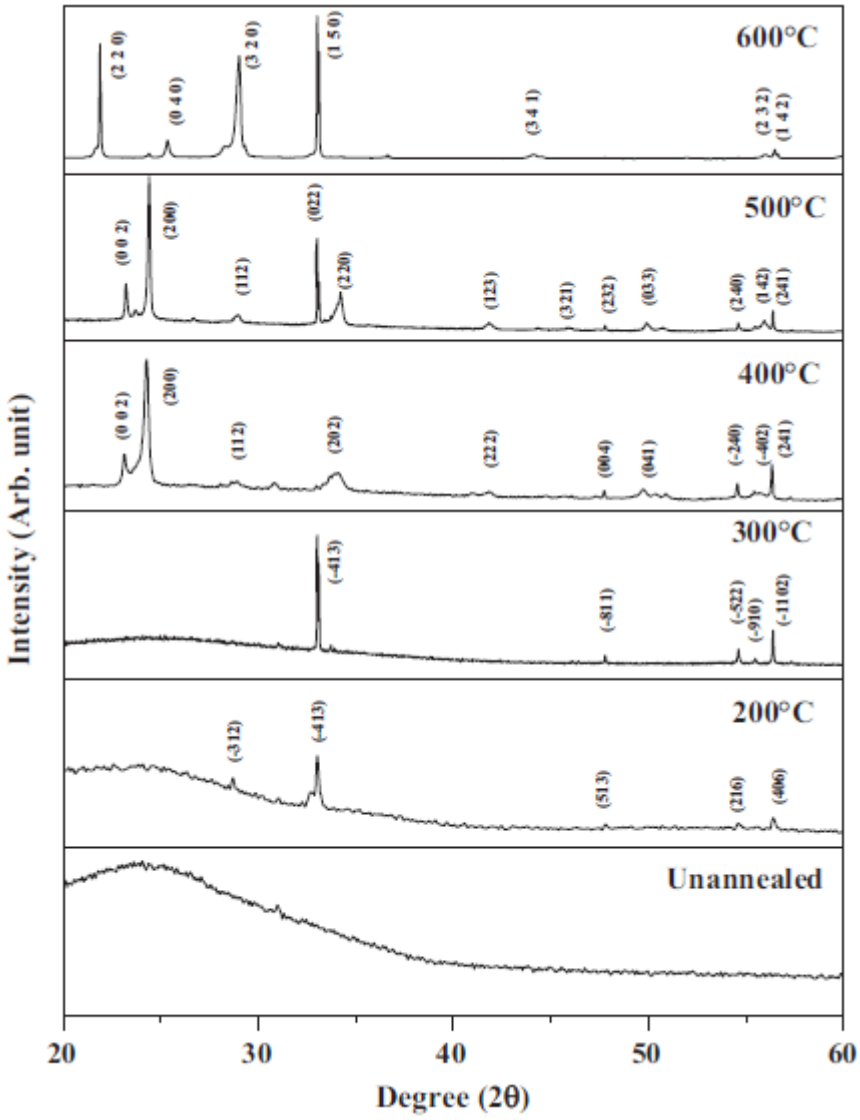

Figure 2.7: The XRD of un-annealed WO_3 and annealed WO_3 at different temperatures, adopted from reference ***[20].***

CHAPTER 3

3. DEPOSITION AND CHARACTERIZATION TECHNIQUES

3.1. Introduction

Since 1960's the technology of thin film surface coatings has been effectively used for different industrial applications and has been researched. Some examples of industrial applications of thin film surface coatings are decorative thin films, hard ware-resistant thin films, low-friction thin films, corrosion-resistant thin films and protective optical systems thin films **[27-28]**. In the research fields, the investigation on thin films has been focused towards understanding the main physical mechanisms such as the interaction between incident charged particles and the surface of target material, the adhesion between a substrate and the deposited material, chemical reactions near the substrate, and the influence of the deposition parameters (substrate temperature, working pressure and the density of power applied to a target) **[28]**.

In recent studies, the deposited materials has been reported to play important role in different applications due to the fascinating properties they exhibited after being deposited as thin films**[20,27-29]**. These thin films also show fascinating structural properties when characterized. The techniques mostly used to characterize thin films are X-ray diffraction, scanning electron microscopy, energy dispersive spectroscopy, atomic force microscopy and Rutherford backscattering spectroscopy. This chapter describes the deposition and characterization techniques used in this study.

3.2. Sputtering deposition technique

Generally, there are various deposition techniques that are utilized for thin film deposition. Some of these techniques are the evaporative method (vacuum evaporation), glow-discharge method (sputtering), gas-phase chemical method (chemical vapour deposition) and the liquid-phase chemical method (electro processes) **[30]**. In this study the sputtering deposition technique was used since this technique is fast (high deposition rate) and ensures good adhesion of clean thin films on the substrates. There are also no unwanted impurities. Sputtering is the ejection of atoms produced by the bombardment of a solid target by energetic particles, mostly ions. It results from the collision between the incident energetic particles and the surface atoms of the target. In sputtering technique, Ar^+ particles (argon ions) are used to bombard a target which acts as a cathode, and the ejected atoms from the target are accelerated to the substrate (anode) where they are deposited as thin films. The measure of the removal rate of surface atoms is the sputter yield *Y* **[31]**, which is defined as a ratio between the number of sputter ejected atoms from the target and the number of incident particles (projectiles). The equation which describes the sputter yield as a function of energy and projectile-target combination has been used by several authors **[31]**. For a given ion mass (projectile mass) and target mass, the yield is given by:

$$Y = \frac{3}{4\pi^2}\alpha\frac{4m_1m_2}{(m_1+m_2)^2}\frac{E}{U_s} \qquad (3.1)$$

where *E* is the energy of the projectile, m_1 and m_2 are the masses of projectile and the target in atomic mass units (a.m.u) respectively, U_s is a binding energy of the target surface and α is a dimensionless parameter which depends on the mass ratio and the energy of ion. Figure 3.1 shows how the sputtering process occurs inside the vacuum chamber. In this process an Ar gas (unreactive

gas) is introduced into the vacuum chamber and is ionized by electric field. The ionized Ar gas (Ar^+) bombards the surface of the metal target producing atoms in plasma form and these atoms are accelerated directly to the substrate where the thin film of metal particles is formed. If oxygen gas (reactive gas) is allowed to enter the chamber it will interact with the atoms of the metal target to form metal oxide and the formed metal oxide is accelerated to the substrate to form a thin film of metal oxide. The sputtering technique allows the control of the sample's stoichiometry by varying the power, the gas flow rate, the temperature, and the time duration of deposition in order to obtain good thin films **[27]**.

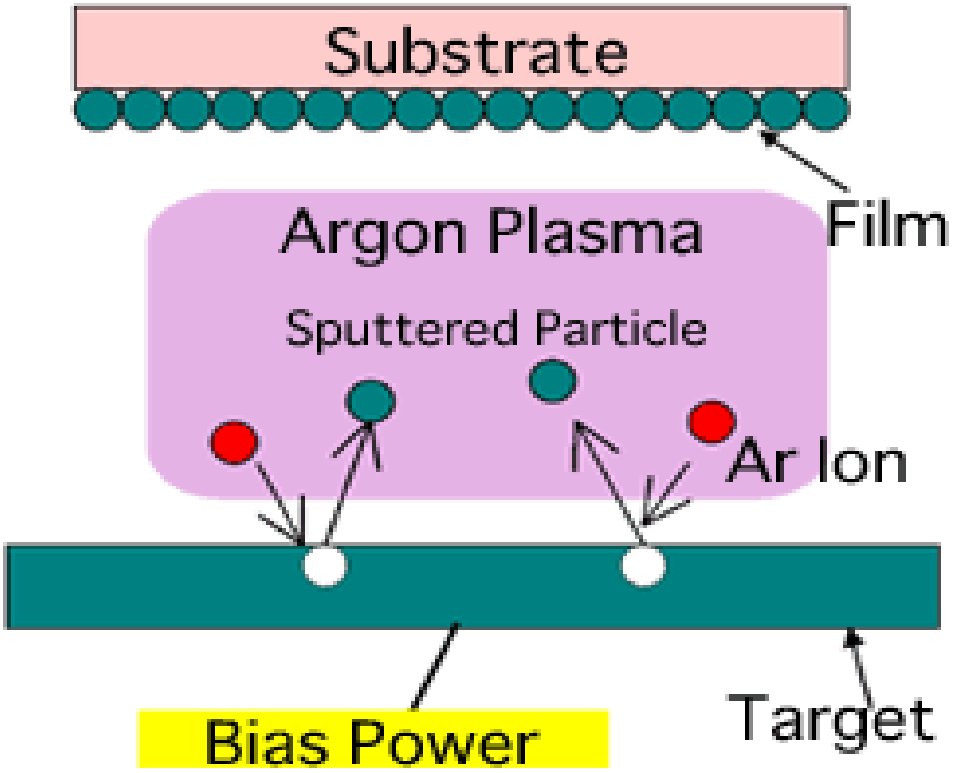

Figure 3.1: The sputtering deposition process occurring inside the vacuum chamber ***[27].***

There are two ways of operating the sputtering deposition process, namely DC (diode) and AC (radio frequency). The two configurations are DC magnetron and RF magnetron sputtering respectively **[28]**.

3.3. DC magnetron sputtering deposition

In DC (diode) discharge there is a cathode and anode electrode. The cathode is the sputtered target and the anode is the substrate. The applied potential in this system appears across the region very close to the cathode and thus the plasma generation region is close to the cathode surface. The cathode in the DC magnetron sputtering must be electrically conductive (metal) since insulating material can develop a surface charge that will prevent ion bombardment of the target surface. The advantage of DC magnetron sputtering is that the plasma can be created uniformly over a large area allowing more target atoms to be ejected **[28]**. However, in DC magnetron sputtering the electrons which are ejected from the cathode are accelerated away from the cathode and are not efficiently used for maintaining the discharge. These effects in DC magnetron sputtering are avoided by a magnetic field which deflects the electrons to a region near the surface of a target. The appropriate arrangement of the magnets in this kind of system cause the electrons to circulate on a closed path near the target surface which creates the high density of plasma from which the ions can be extracted to sputter or bombard the target (cathode). The target material is placed above the magnets in the shutters **[28,30-32]**. Figure 3.2 below shows the process occurring in DC magnetron sputtering.

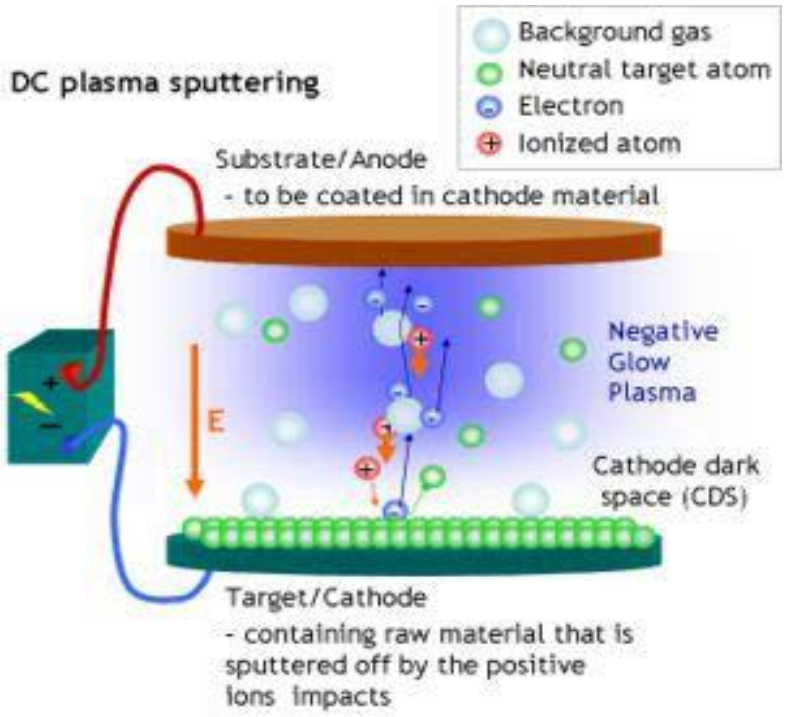

Figure 3.2: The sputtering process occurring in DC magnetron sputtering ***[27].***

3.4. RF magnetron sputtering deposition

The RF (radio frequency) magnetron sputtering can be used to sputter an insulating material using RF power to form thin films on the substrates **[28,32]**. In Figure 3.3 below the configuration of RF magnetron sputtering is illustrated. It shows how the process occurs in the system. RF magnetron sputtering operates at a frequency of about 13.5 kHz **[27]**. The important advantage of RF sputtering is that a high voltage can be applied to the target for a long period of time without any discharge occurring **[27]**. In a proper configuration for the target and the substrate in RF powered systems, the substrate electrode is made to be much larger than the target electrode by electrically connecting the substrate table to the entire system. The disadvantage of the RF powered systems is the low deposition rate **[31]**.

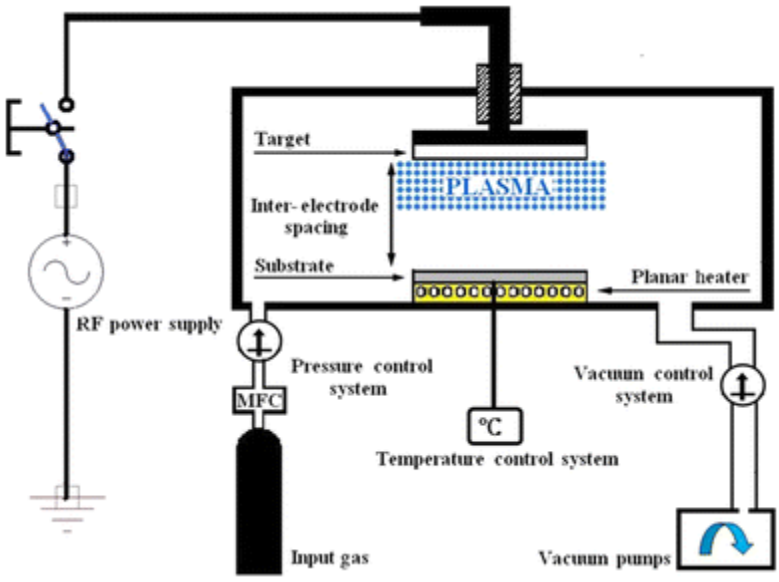

Figure 3.3: The sputtering process in RF magnetron sputtering ***[33].***

3.5. Characterization techniques

After the target material has been deposited onto the substrate where the thin film is formed, the properties of the thin film (crystallinity, morphology, composition, surface roughness and thickness) is investigated. In this study the characterization techniques like X-ray diffraction, scanning electron microscopy, energy dispersive spectroscopy, atomic force microscopy and Rutherford backscattering spectroscopy were utilized to investigate the properties of the deposited thin films.

3.6. X-ray diffraction (XRD)

The X-ray diffraction technique is one of the best known technique used to characterize samples of materials like thin films. The XRD technique can be used for phase identification, crystal structure determination, thin film quality measurements, crystallographic texture observation, percent crystalline/amorphous determination, crystal size analysis, defect studies, residual stress/strain identification, phase transitions observation, and super lattice structure identifications.

In Figure 3.4 below is the image of X-ray diffraction that was used in this study to characterize thin films of WO_3. X-ray diffraction monochromatic radiation is used to interact with the sample. The sample is probed with monochromatic X-rays of a known wavelength in order to evaluate the d-spacing of the crystal sample according to Bragg's law **[27,34]**.

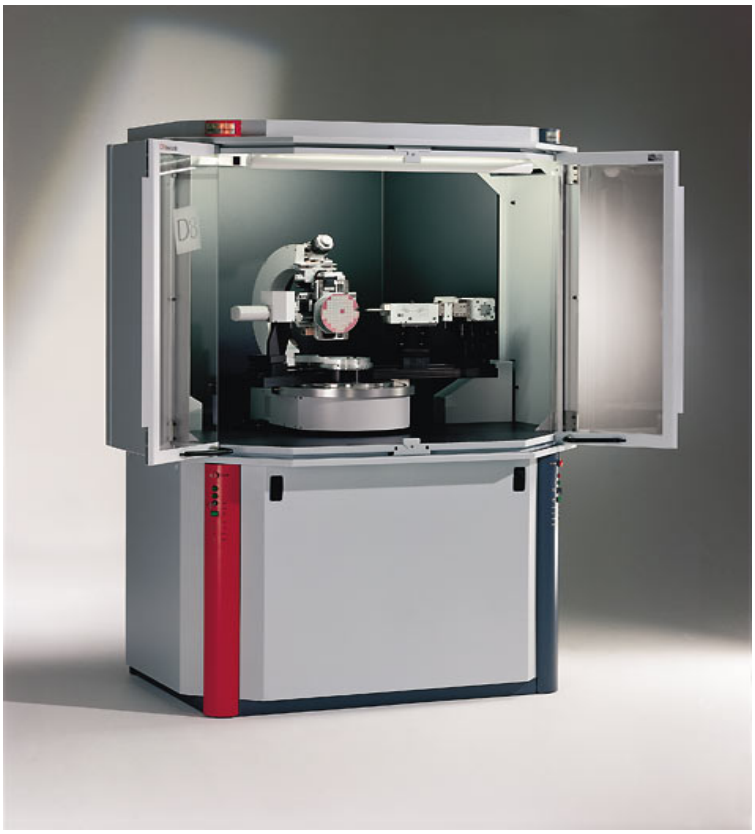

Figure 3.4: Bruker's X-ray diffraction D8-Discover instrument ***[35].***

In Figure 3.5 below the basic diffractometer set up is shown. It shows the geometry of the process occurring inside the diffractometer as the X-rays interact with the target sample. X-rays are generated from the X-ray tube. The X-ray tube is stationary and the sample rotates by the angle θ, and the detector detects the scattered beam of X-rays from the sample at the angle 2θ. The detector records the intensity of the scattered beam of X-rays and the diffraction peaks of the sample are observed on the computer screen.

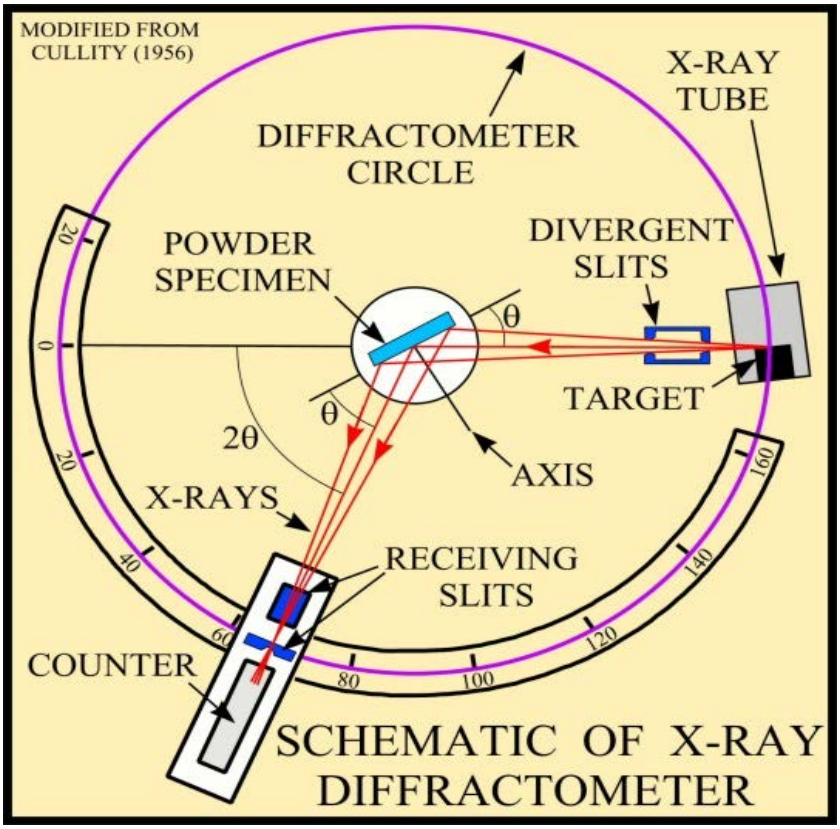

Figure 3.5: Schematic of the basic X-ray diffractometer set up ***[34].***

3.7. Production of X-rays

X-rays are generated in the X-ray tube by colliding energetic electrons with a metal target. Figure 3.6 shows the X-ray tube and process taking place inside for the generation of X-rays. In the X-ray tube the tungsten filament is the source of electrons, the metal target material is the anode. The tube voltage accelerates the electrons to strike the metal target and interact with electrons in the atoms of the metal target to produce X-rays. Electrons lose energy through ionization and radiative collisions in the target material. Energetic incident electrons strike the electrons in atoms of the target and the electrons from the higher energy levels fill the vacancy, and these transitions result

in the emission of X-rays. The X-ray energy is determined by the anode material, accelerating voltage and monochromators. The energy can be given as:

$$E = hv \qquad (3.2)$$

where *h* is Planck's constant and *v* is the frequency of the X-ray **[34]**. The energy of emitted X-rays from atoms of the target (metal) is the energy difference between the lower level (inner shell) energy and the high energy level of the transition. During the de-excitation of electrons in the atomic shells of the target, two types of X-ray radiations are generated, namely, the characteristic X-rays and the bremsstrahlung **[36]**.

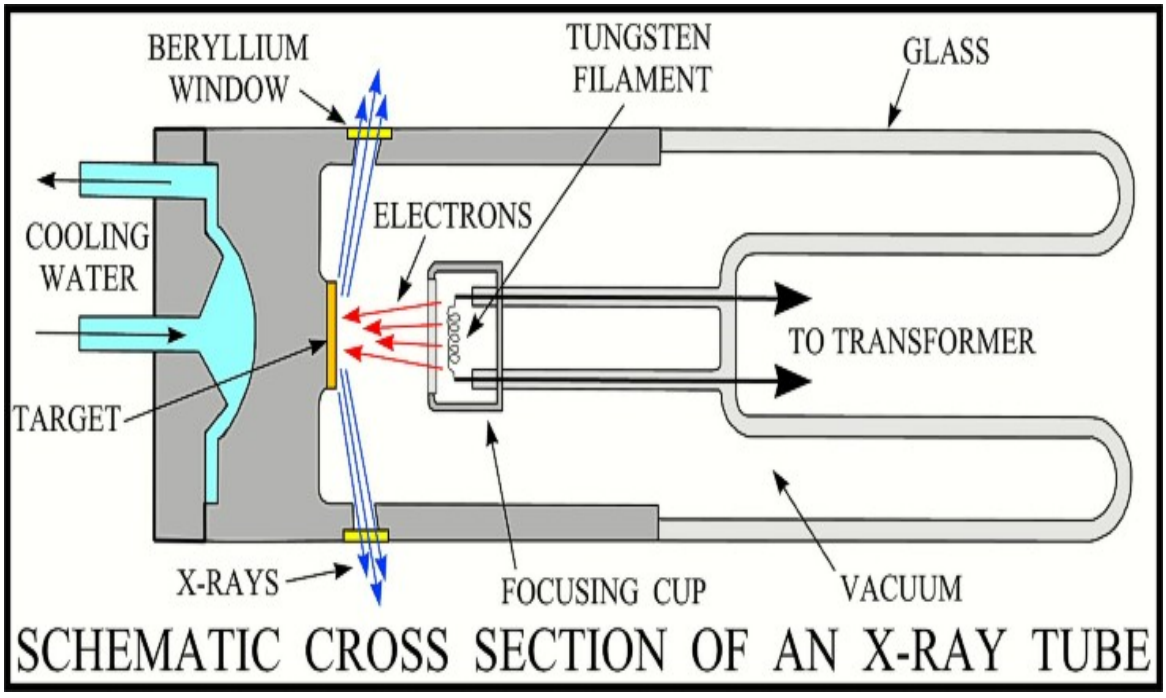

*Figure 3.6: Schematic cross section of the X-ray tube for generating X-rays **[34].***

Characteristic X-ray radiation occurs when the electron from the filament displaces the electron from an inner-shell of the metal target atom and ionizing the atom. Metal target can be tungsten, copper, or other metals in the X-ray tube. When this process occurs, another electron in an outer-shell of target atom is quickly attracted into the vacant in an inner-shell. When the displaced electron is replaced by the electron from the outer-shell a photon is emitted. The energy of emitted photon is equivalent to the difference between the initial and final states corresponding to the difference between two orbital binding energies. The emitted photon is called characteristic X-ray. Characteristic X-ray has a higher intensity and it can be modified by altering the tube voltage and tube current in order to suit the needs of the application **[36]**. Figure 3.7 shows how the characteristic X-ray radiation is generated.

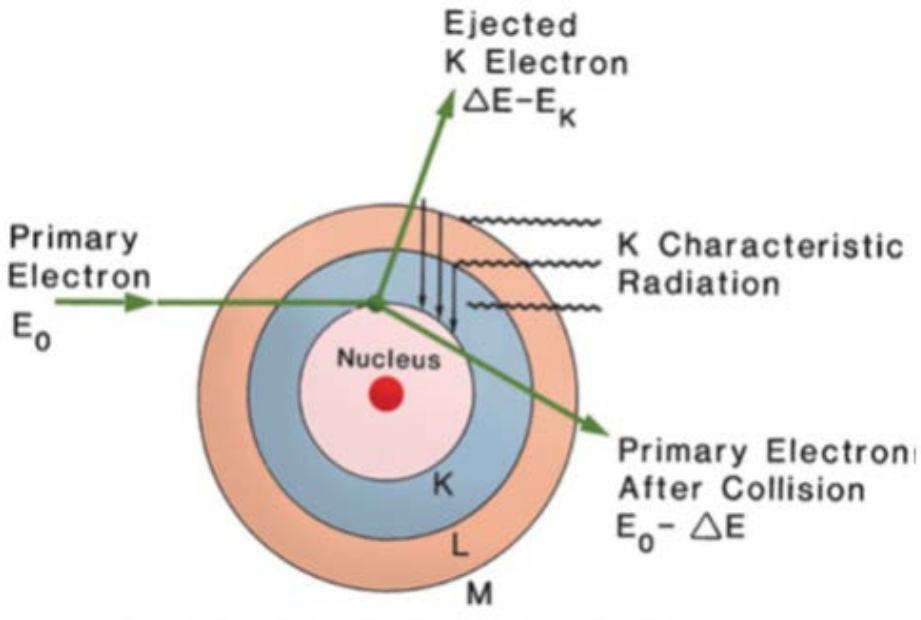

Figure 3.7 Schematic representation of characteristic X-ray generation ***[37].***

Another type of radiation that can occur is Bremsstrahlung radiation, this radiation is produced by the sudden stopping, or slowing down of high-speed electrons in the target. Most of the high-speed electrons have near or wide misses with the nuclei. In these interactions, a negatively charged high-speed electron is attracted toward the positively charged nucleus and then loses some of its velocity. This kind of deceleration causes the electron to lose some of its kinetic energy which is then given off in the form of a photon. When a high-speed electron comes close to a nucleus, it experiences greater electrostatic attraction which can result in greater energy of the Bremsstrahlung photon **[36]**. Figure 3.8 shows how the Bremsstrahlung radiation is generated.

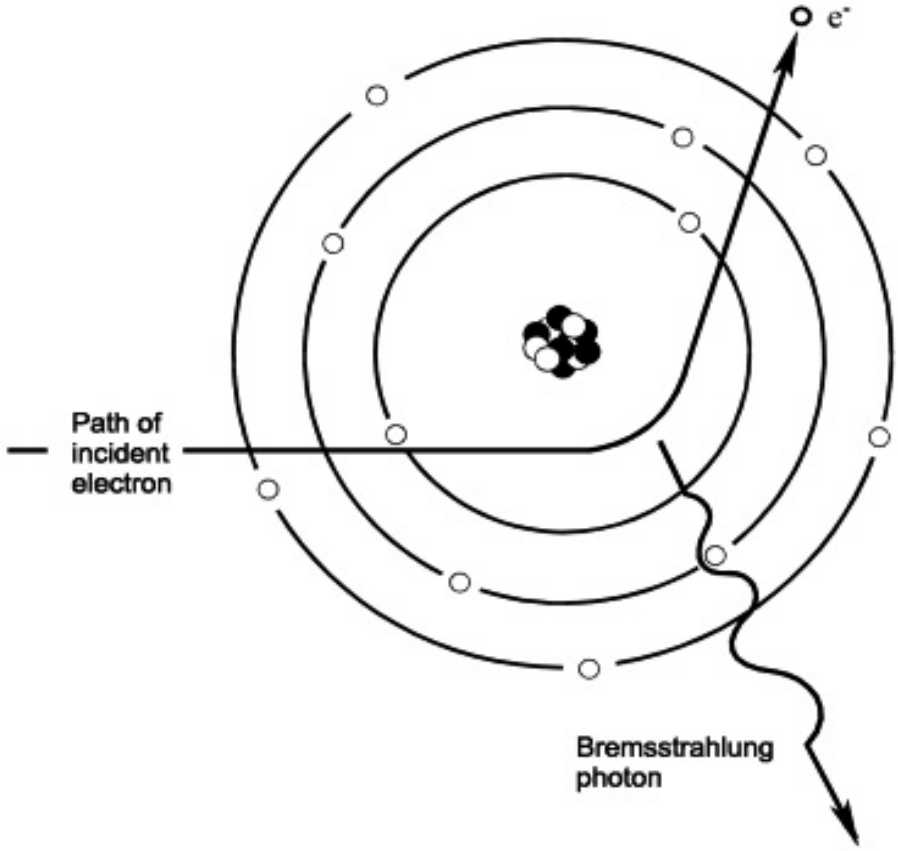

*Figure 3.8 Schematic representation of generation of Bremsstrahlung radiation **[38]**.*

3.8. Bragg's law of diffraction

After X-rays are generated from the X-ray tube, they can be directed to the sample for characterization purpose. The sample can either be a crystalline or amorphous. The crystalline sample have a periodic arrangement of atoms but in an amorphous sample there is no specific arrangement of atoms. Interaction of X-rays with the sample is described by the Bragg's law, **[34]** which is presented in equation (3.3). The interaction of incident X-rays with the crystalline sample is illustrated in Figure 3.9. The incident X-rays are reflected on the parallel atomic planes of the sample. These planes are separated by -inter planar spacing, d. The X-rays produce constructive interference of scattered X-rays from the sample only if the condition for constructive interference is precisely met. This condition satisfies the Bragg's law

$$n\lambda = 2d_{(hkl)} \sin \theta_B \qquad (3.3)$$

where $n\lambda$ is the phase difference, n is an order of diffraction, λ is the wavelength of the X-ray, θ_B is the angle of incident X-ray (Bragg angle) and $d_{(hkl)}$ is the interplanar spacing. The set of integers h, k, and l is the Miller indices which gives the crystallography of atomic planes in a crystalline sample. The diffracted X-rays from the sample are detected by an X-ray detector in order to be processed and counted. Diffracted X-rays carry information about the sample and each diffraction peak is associated with a set of Miller indices. In amorphous samples no diffraction peaks will be observed because constructive interference does not occur on it **[35]**. The conversion of the diffraction peaks to the inter-planar spacing d allows the identification of the sample since each sample has a unique set of inter-planar spacings **[35]**. For each set of Miller indices (*hkl*) corresponding to each diffraction peak, the inter-planar spacing for different crystal systems of the

samples can be calculated as shown in Figure 3.10, where *a*, *b* and *c* are the lattice constants corresponding to a crystal structure of the sample.

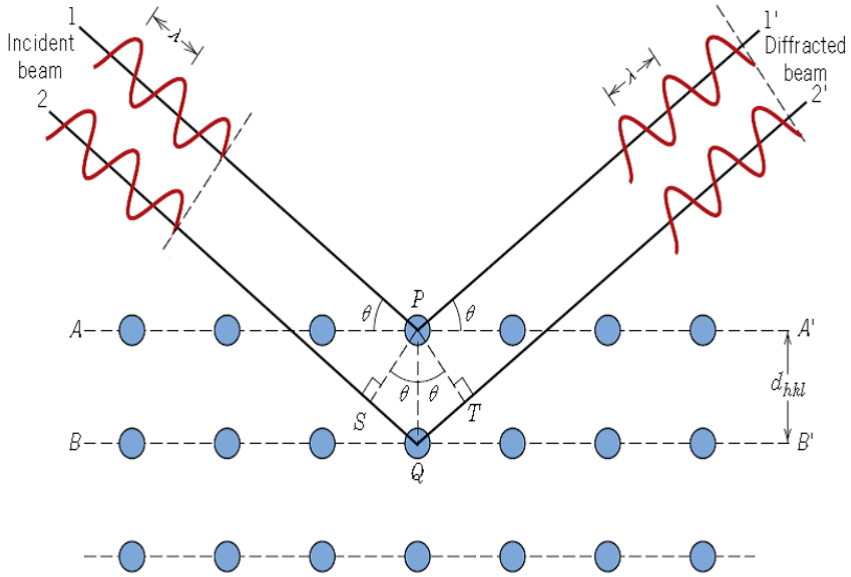

Figure 3.9: Interaction of incident X-ray beam with the crystalline sample ***[34].***

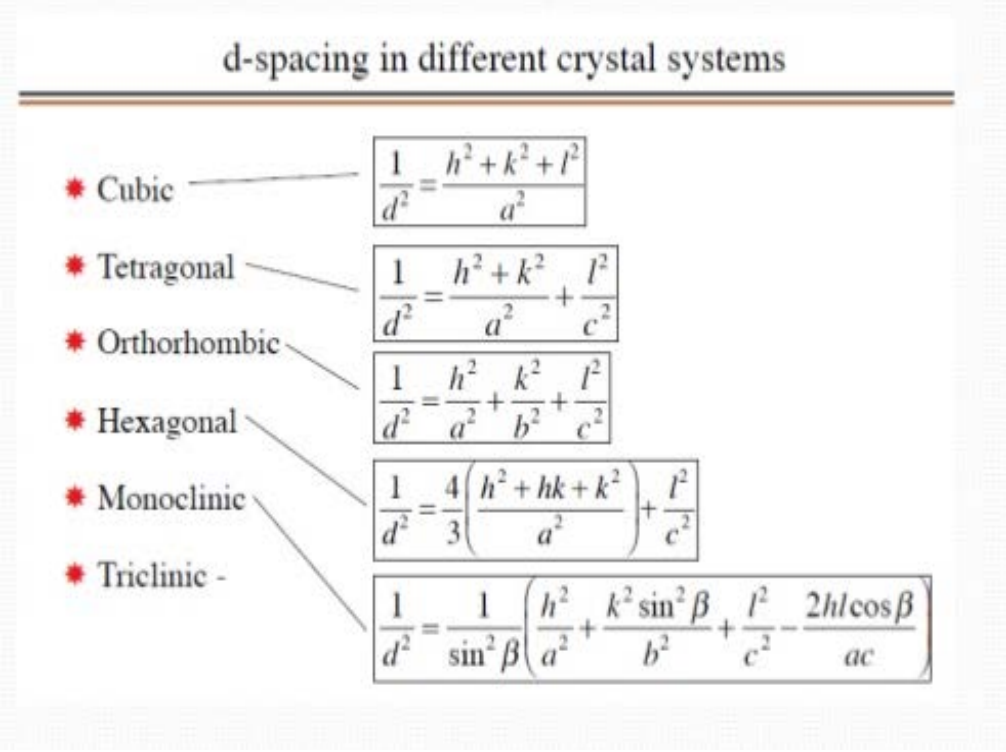

Figure 3.10: The d inter-planar spacings for different crystal structure systems.

3.9. Scanning electron microscope (SEM)

The SEM technique equipped with EDS is widely used in industry and laboratories to study microstructures, surface morphology, elemental mapping, and chemical composition of materials **[32,39]**. Figure 3.11 shows the SEM of the University of Zululand in the Physics and Engineering Department. The main components of SEM, as shown in Figure 3.12 are the electron source (electron gun), microscope column, magnetic lenses, scanning coils, electron detectors, sample chamber, computer and display screen to view the images **[32,40]**. Electrons produced from the electron gun at the top of the column are accelerated and pass through magnetic lenses and apertures to form a focused beam which is directed to the sample surface (specimen). Electrons are backscattered from the sample and are detected **[39]**. The sample is mounted on a stage in the chamber. The scanning electron microscope is designed to operate at high vacuum and therefore a

series of pumps are utilized to achieve high vacuum. The vacuum system includes fore-vacuum and turbo pumps. The position of the electron beam on the sample is controlled by scanning magnetic coils. These coils allow the beam of electrons to be scanned over the surface of the sample **[39-40]**. As the electrons interact with the sample, signals are produced and these signals are then detected by appropriate detectors to form images of the sample. EDS is usual connected to the SEM to give the elemental composition **[39]**.

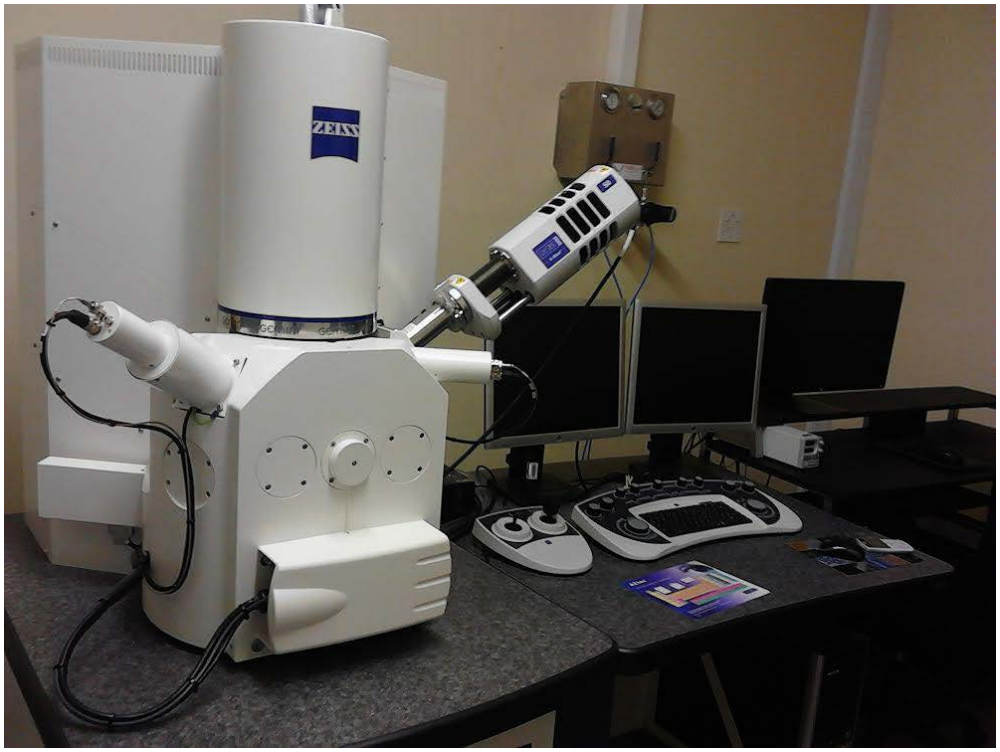

Figure 3.11: SEM of the University of Zululand in the Physics and Engineering Department.

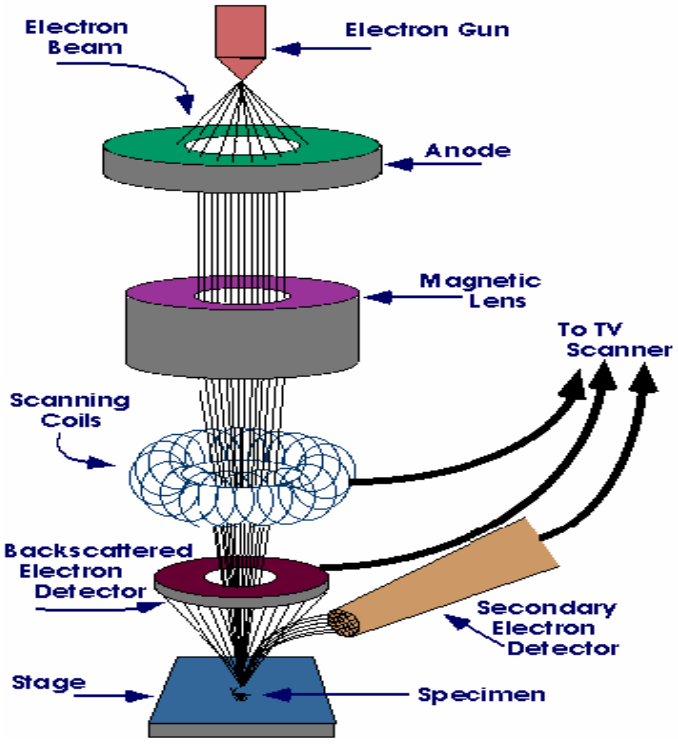

Figure 3.12: Schematic illustration of the basic components of the SEM ***[40].***

When the incident electron beam hits the surface of a sample (specimen), many electron scatterings can occur, as shown in Figure 3.13 **[41]**. Secondary electron scatterings do occur and these are mainly due to electrons that are ejected by the sample surface during the interaction of the incident electron beam with the sample surface **[40]**. Some incident electrons can be reflected from the sample surface and those electrons are referred to as backscattered electrons. They can be detected by the backscattered electron detector. Some incident electrons are absorbed by the sample and those are called primary electrons. The absorption of electrons by the sample results in X-ray radiation, following de-excitation of electrons in the sample. This radiation is characteristic of the elements present in the sample. Therefore the X-ray detector utilized in the SEM provides the information of the composition of the sample **[40]**. Backscatter and secondary electron detectors provide more information about the surface morphology of the sample **[39-41]**. An Auger electron

is emitted when the atom of the sample is in an excited state and undergoes a transition to a lower state **[40]**.

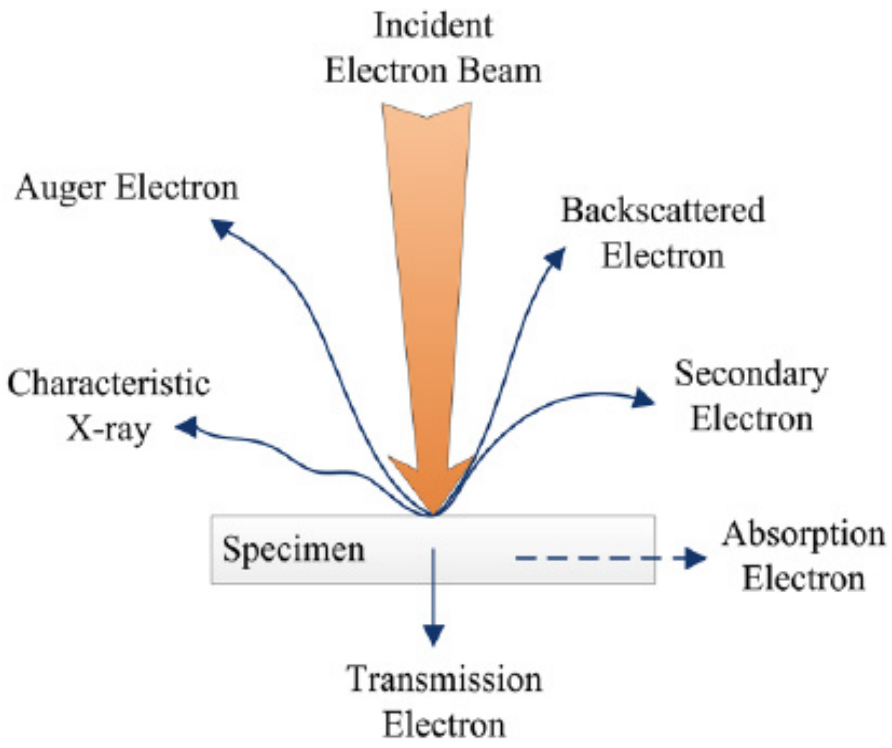

Figure 3.13: Schematic representation of the interaction of the incident beam and radiation signals generated during interaction ***[41].***

3.10. Atomic force microscope (AFM)

AFM is a type of scanning probe microscope (SPM) which forms images of surfaces. It uses a physical probe that scans the sample **[42-43]**. AFM is based on the attractive-repulsive electromagnetic force between atoms in the surface of the sample and atoms in the AFM tip

(probing tip attached to a cantilever-type spring) **[43]**, as shown in Figure 3.14. The interaction force causes the cantilever to deflect following Hooke's law

$$F = K_c \delta \qquad (3.4)$$

where δ, is the cantilever deflection (measured in nm) and K_c is the spring constants (N/m), which normally ranges from 0.03 to 5 N/m resulting in forces from pico Newton (pN) to micro Newton (μN) in ambient conditions **[42]**. As the probe scans the sample, the variations in the surface topography cause changes to the interaction force and therefore in the angular displacement of the cantilever. As the AFM tip scans the sample, topographical features on its surface result in changes of the position of a laser spot on a photodiode detector. The detector is a part of a feedback loop employed to maintain a constant deflection or a constant force between the tip of the AFM and the sample by altering the voltage applied to the scanner **[42]**. In AFM, there are two force regimes involved and are distinguished as contact and non-contact mode **[42-43]**. When the AFM is operated in non-contact mode at tip-sample separations of 10 to 100 nm, forces such as Van der Waals, electrostatic, magnetic or capillary forces, can be sensed and give information about the surface topography, distributions of charges, magnetic domain wall structure or liquid film distribution **[43]**. At the smaller separations of the order of nanometers (nm) the probing tip is in contact with the sample. In this mode, the ionic repulsion forces allow the surface topography to be traced with high resolution. Under best conditions atomic resolution is achieved **[42-43]**.

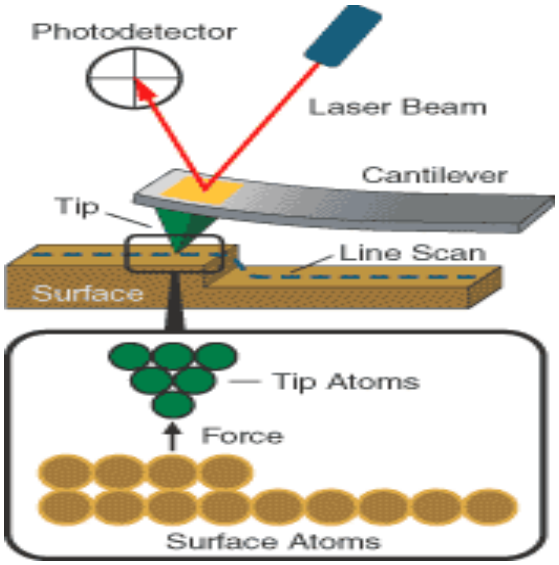

Figure 3.14: Schematic illustration of an atomic force microscope as it scans the sample ***[42].***

3.11. Rutherford Backscattering Spectrometry (RBS)

Rutherford backscattering spectrometry (RBS) is one of the best elemental analysis techniques, where the incident alpha particles (He) are directed to the target and then scattered off the target. This technique is used to determine elemental composition and thin film thickness **[44,45]**. A target is bombarded with alpha particles which have energy in the MeV range (typically 0.5-4 MeV), and the energy of the backscattered projectiles is recorded with an energy sensitive detector (solid state detector) **[44]**. The advantages and disadvantages of RBS **[44]** are as follows:

Advantages of RBS

- RBS is quantitative without the need for reference samples
- RBS is non-destructive
- RBS has a good depth resolution of the order of several nanometers
- RBS has good sensitivity for heavy elements; of the order of parts-per-million (ppm).

Disadvantages of RBS

- RBS has low sensitivity for light elements, which then requires the combination of other nuclear based methods e.g. nuclear reaction analysis (NRA) or elastic recoil detection analysis (ERDA).

Figure 3.15 shows the schematic illustration of an ion (alpha particle) which is scattering from a surface atom of the target. In this Figure, an ion of mass m_1 and kinetic energy E_0 with velocity v_0 is incident at an angle α on a target with mass m_2. The ion is scattered through an angle θ with respect to the incident direction, losing part of its kinetic energy to the target atom during a collision. The scattered ion has the kinetic energy E_1 and velocity v_1 while the target atom recoils with a kinetic energy E_2 and velocity v_2 at angle φ with respect to the incident direction **[46]**.

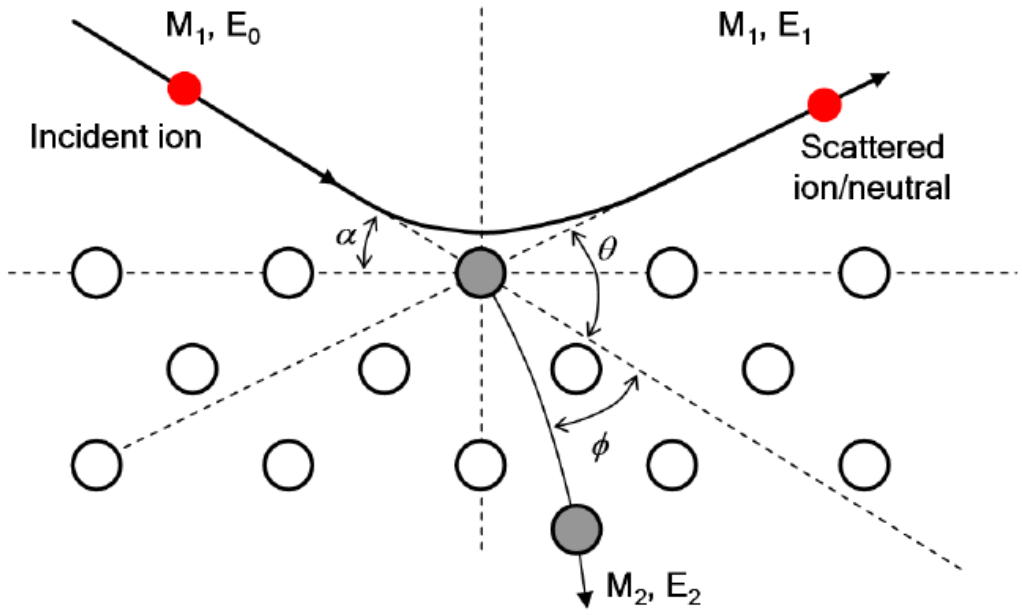

Figure 3.15: Schematic illustration of Rutherford backscattering process for incident ion of mass m_1 and the target of mass m_2 ***[46].***

When assuming that the collision shown in Figure 3.15 is elastic, the conservation of both the kinetic energy and the momentum are considered to obtain the following:

$$m_1 v_0^2 = m_1 v_1^2 + m_2 v_2^2 \qquad (3.5)$$

By rearranging equation (3.5) of conservation of kinetic energy leads to:

$$m_2 v_2^2 = m_1 (v_0^2 - v_1^2) \qquad (3.6)$$

The conservation of momentum parallel to the incident direction can be written as:

$$m_1 v_0 = m_1 v_1 \cos\theta + m_2 v_2 \cos\varphi \qquad (3.7)$$

The momentum perpendicular to the incident direction can be written as:

$$0 = m_1 v_1 \sin\theta - m_2 v_2 \sin\varphi \qquad (3.8)$$

As in **[46]**, these equations can be rearranged and added up until the ratio of the scattered alpha particle's energy E_1 to its incident energy E_0 is obtained, as follows:

$$k = \frac{E_1}{E_0} = \left[\left(\frac{1}{m_1 + m_2}\right)\left(m_1 \cos\theta \pm \sqrt{m_2^2 - m_1^2 \sin^2\theta}\right)\right]^2 \qquad (3.9)$$

k is the kinematic factor equals to the ratio E_1/E_0 as shown in equation (3.9), the kinematic factor gives the convenient method for determining the elemental composition which makes up the target atoms **[45]**.

Figure 3.16 shows how the thickness (Δx) of a thin film of a target is obtained from the obtained RBS spectrum of the thin film target,

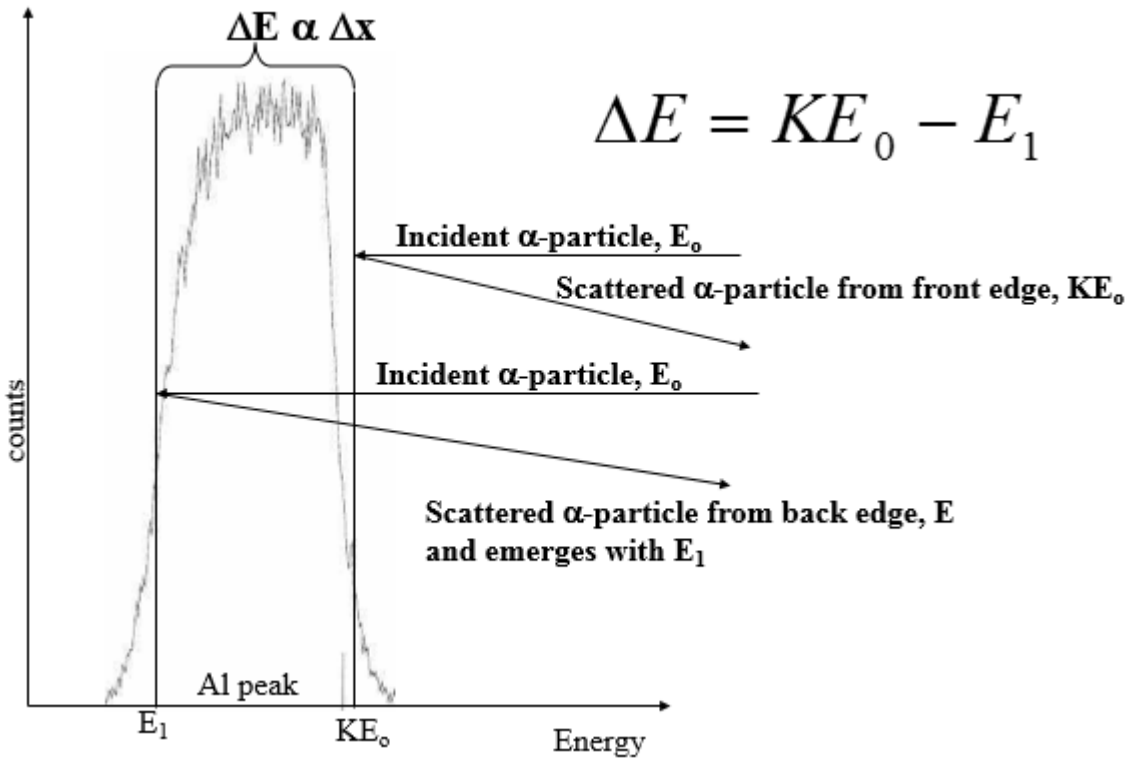

*Figure 3.16 Thickness determination from a thin film **[45].***

The thickness of the thin film being analysed can be calculated as in **[45]**, using the equation (3.10) below:

$$\Delta x = \frac{\Delta E}{S_0} \qquad (3.10)$$

where S_0 is the energy loss factor which involves the stopping power of the alpha particle as it travels through the target.

CHAPTER 4:

4. SYNTHESIS AND CHARACTERIZATION OF THIN FILMS OF WO_3 NANOSTRUCTURES

4.1. Sample preparation

The thin film nanostructures of WO_3 were prepared on glass, silicon (111) and alumina strip substrates using an AJA orion 5 DC magnetron sputtering system shown in Figure 4.1, at the University of Zululand. The substrates (glass and silicon) were first cleaned chemically using methanol, acetone, trichloroethylene, and finally repeated with methanol for 5 minutes each in an ultrasonic bath. The substrates were then rinsed with distilled water and dried using dry nitrogen. They were then loaded on the sputtering machine in the vacuum chamber as shown in Figure 4.2. The control panel unit shown in Figure 4.2 was used to set and control all parameters used for deposition. Samples were prepared in the vacuum chamber. The chamber was first evacuated to a pressure of 2×10^{-7} Torr to avoid unnecessary impurities such as gases. The temperatures were varied during each deposition to ensure the formation of crystalline WO_3 nanostructures. WO_3 was deposited from the sputtering of W (99.9% purity) target in an $Ar+O_2$ plasma environment as shown in Figures 3.1 and 3.2 of Chapter 3. The tungsten (W) target was placed in the vacuum chamber in shutter 1 as indicated in Figure 4.2 (during deposition the shutter was opened in order to expose the W target to the bombarding particles). Argon (Ar) was used for sputtering since it is a noble gas. There are many oxides of tungsten but WO_3 is the most stable oxide and therefore during the deposition of magnetron energy, flow rates of both Ar and O_2 and temperature were varied to obtain the required oxide (WO_3). Sputtering was done for the period of one hour at a pressure of 3×10^{-3} Torr, to ensure deposition on the substrates. Samples were then allowed to cool in vacuum before being removed from the vacuum chamber.

Figure 4.1: The AJA orion 5 DC magnetron sputtering system for deposition at the University of Zululand, Department of Physics and Engineering.

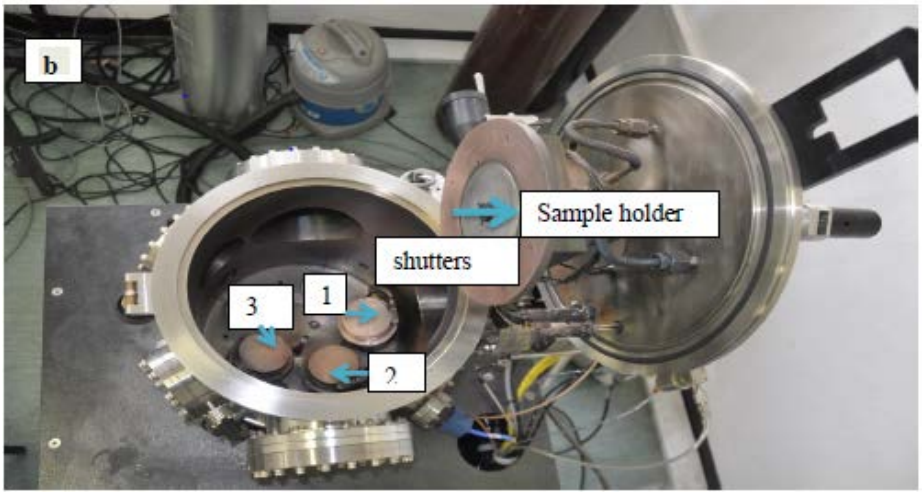

Figure 4.2: The internal parts of the vacuum chamber showing three shutters labelled 1, 2 and 3, where 1 is for balanced magnetron depositions using DC power supply suitable for deposition of metals, 2 for unbalanced magnetron deposition using DC power supply suitable for deposition of magnetic materials, and 3 for the RF magnetron for deposition of ceramics materials.

4.2. Synthesis of thin films of WO_3 nanostructures

WO_3 nanostructures were synthesized on silicon wafers (111), glass and alumina substrates using the DC magnetron sputtering technique where a 99.9% pure tungsten target as purchased from AJA was deposited at a pressure of 3×10^{-3} Torr for 1 hour. The optimum synthesis condition for WO_3 nanostructures was reached by varying the deposition power between 100 W to 200 W in steps of 50 W, the oxygen flow between 2 to 8 sccm and the deposition temperatures between 300 ℃ and 500 ℃. RBS and XRD characterization techniques revealed that the best synthesis parameters to synthesize WO_3 nanostructure thin films is the deposition power of 150 W, Argon gas flow rate of 8 sccm, while the Oxygen gas flow is 6 sccm and the deposition pressure of 3 x 10^{-3} Torr for a deposition time of 1hour The deposition temperature was varied between 300 ^oC to 500 ^oC. Subsequently to preparing these WO_3 nanostructure samples at 300 ^oC, 400 ^oC and 500 ^oC, all necessary characterization techniques were carried out.

4.3. CHARACTERIZATION OF THIN FILMS OF WO_3 NANOSTRUCTURES

4.3.1 SEM analyses of WO_3 thin films

Figure 4.3 (a-c) shows the SEM images of WO_3 nanostructure thin films that were deposited on silicon substrates by DC magnetron sputtering at different deposition temperatures (as explained in Section 4.2). Figure 4.3 (a), (b) and (c) are of WO_3 films prepared at 300, 400 and 500 ℃ respectively. During the deposition of WO_3 films all other parameters were maintained unchanged except for the deposition temperature and therefore it can be concluded that as the temperature changes the morphology of WO_3 film also changes. When the temperature was 300 ℃, the WO_3 film seems to exhibit evenly distributed small spherical particles, at 400 ℃ it exhibited a film of

many granules which were different in shape compared to those where temperature was 300 ℃, and at 500 ℃ the morphology ofthe film changed to particles of shape similar to cornflakes.

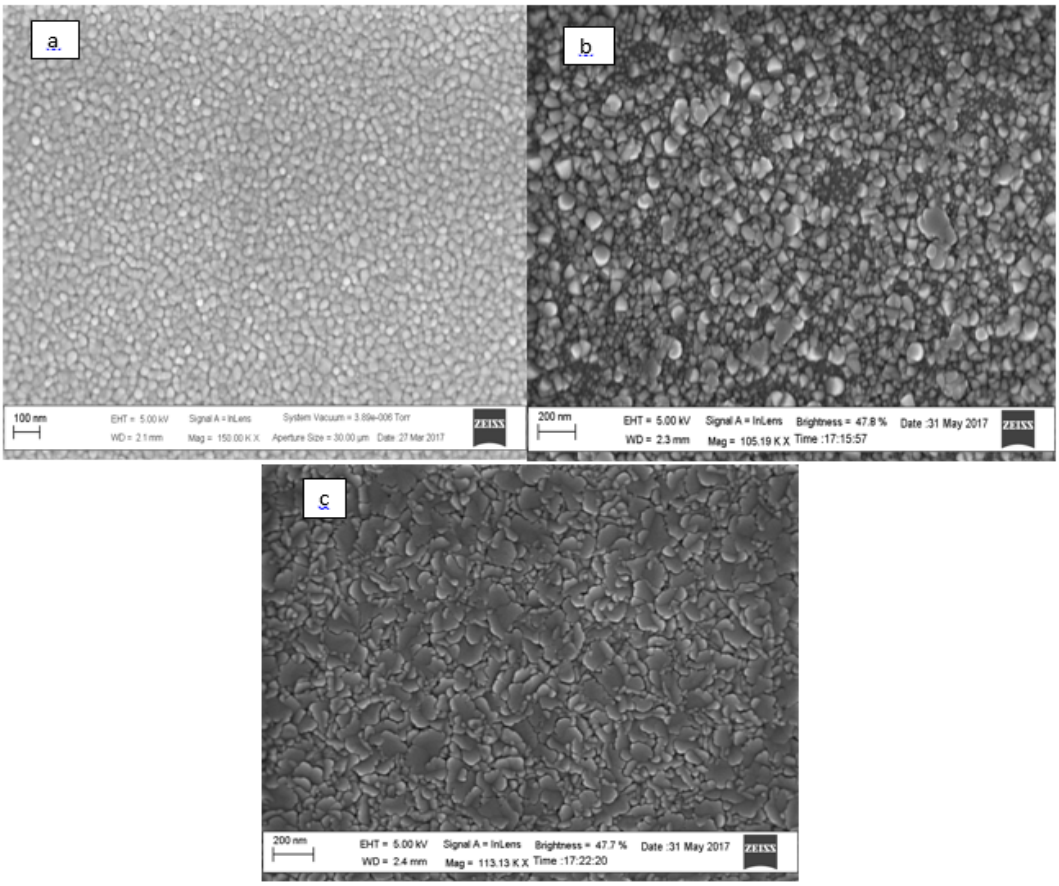

Figure 4.3: The SEM images of thin film WO_3 nanostructures deposited at different temperatures (a) 300 ℃, (b) 400 ℃and (c) 500℃It is evident from these results that as the temperature changes the morphology of the thin film WO_3 nanostructures also changes.

4.3.2. XRD analyses of WO3 thin films

Figure 4.4 (a-c) shows the XRD spectra of the WO_3 nanostructure thin films that were prepared by DC magnetron sputtering as explained in Section 4.2. The samples were prepared at different temperatures (300, 400 and 500 ℃). The X-ray diffraction patterns indicated by letters a, b and c

are of WO_3 prepared at 300, 400 and 500 ℃ respectively. In figure 4.4, it can be observed that the change in deposition temperature has resulted in the structural and phase transformation in WO_3 thin films. In figure 4.4 (a), WO_3 is amorphous (pdf card number: 01-089-8764) since no diffraction peaks was observed or no x-ray diffraction was detected. In figure 4.4 (b) the phase change of WO_3 was observed from amorphous to hexagonal (pdf card numbers: 01-089-4476) at 400 ºC, WO_3 is polycrystalline and a sharp diffraction peak was observed at 2θ = 33.22º, corresponding to the (112) plane which indicates a fine preferential growth in the (112) direction. In figure 4.4 (c) WO_3 is polycrystalline, the phase change from hexagonal to tetragonal phase (pdf card number: 01-085-2460) was also observed at 500 ºC and the strongest diffraction peak was observed at 2θ = 23.71º corresponding to the (001) plane which indicates a fine preferential growth in the (001) direction. The last peak on the right hand side of figure 4.4 is the peak from the silicon substrate. The increase in temperature resulted in the formation of different phases and orientations in WO_3. The diffraction peaks tended to be sharper as the deposition temperature increased, which corresponds to an increase in particle size **[10]**. The crystallite sizes or grain sizes for each of the WO_3 sample prepared at different temperatures were estimated using the diffraction peaks corresponding to the (112) and (001) planes for WO_3 prepared at 400 ºC and 500 ºC respectively according to Scherrer's equation 4.1 **[10]**:

$$D = \frac{0.9\lambda}{B\cos\theta} \qquad (4.1)$$

Where D is the mean grain size, B is the full width at half maximum (FWHM). This is the line broadening at half the maximum intensity of the peak which can also be denoted as $\Delta 2\theta$, where θ is measured in radians, λ is the wavelength of the X-rays and θ is angle at the centre of the peak called Bragg's angle (in degrees), for 300 ºC film they is no peak to use Scherrer's equation. The X-ray wavelength (Cu $K_\alpha 1$, $\lambda = 0.15406$ nm) was used and the FWHM was calculated using the

origin for each peak. The sharper the diffraction peak indicating an increase in grain size as it can be observed in Table 4.1.

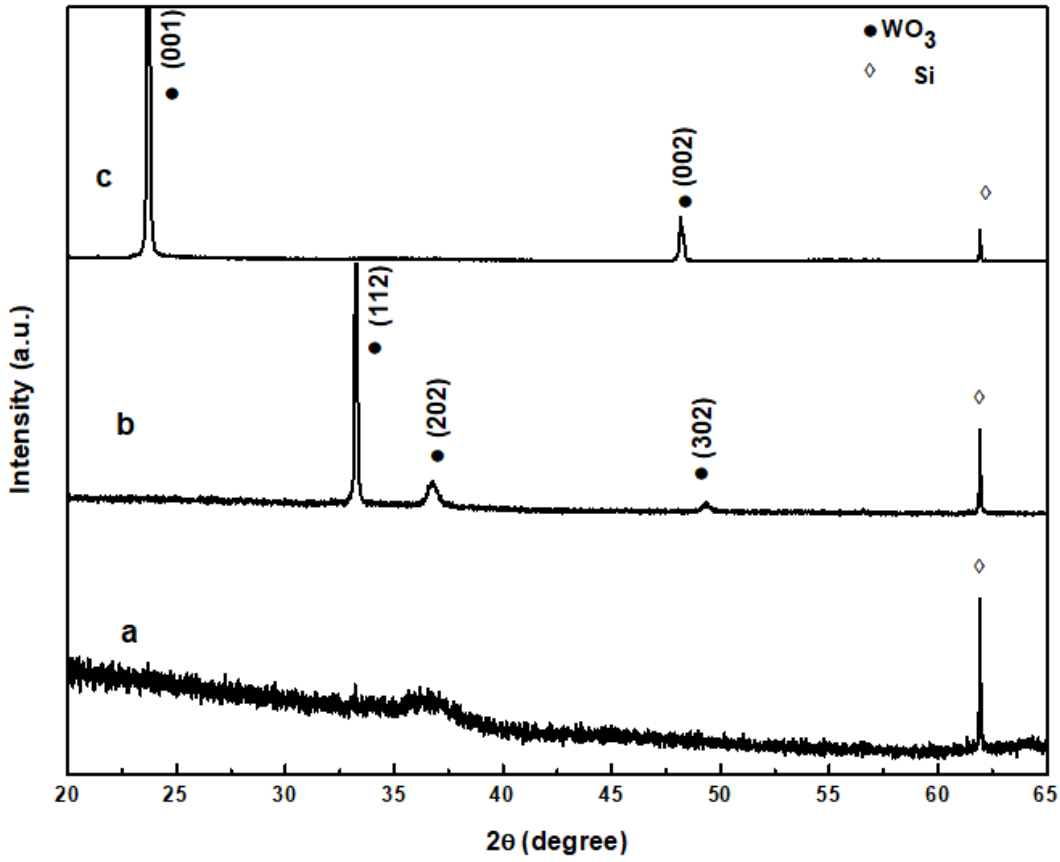

Figure 4.4: The XRD patterns of WO_3 prepared by DC magnetron sputtering at different temperatures (a) 300 ℃, (b) 400 ℃and (c) 500 ℃

Table 4-1: The grain size of WO_3 prepared by DC magnetron sputtering at different temperatures

Annealing Temperature (◦C)	B (FWHM) (radians)		Grain size (nm)	
Planes:	(112)	(001)	(112)	(001)
300 ℃	-	-	-	-
400 ℃	$3x10^{-3}$	-	48.23 nm	-
500 ℃	-	$2x10^{-3}$	-	70.84 nm

4.3.3. AFM analyses of WO_3 thin films

Figure 4.5 shows the surface topography of the WO_3 nanostructure thin films in 3-dimencions, obtained using the AFM technique (contact mode). The films were prepared by DC magnetron sputtering on silicon substrates at various temperatures: (a) 300 ℃, (b) 400℃ and (c) 500 ℃ as labelled in Figure 4.5 respectively. A scan range of 1.6 µm was used for the samples shown in Figure 4.5 (a) and (b), and the scan range of 2.5 µm illustrated in Figure 4.5 (c) was used since the surface topography was easily obtained. It indicated that the sample consisted of large particles compared to the others (where the WO_3 thin film was prepared at 300 and 400 ℃). The values are presented in Table 4.2. The average roughness and the average particle size distribution of WO_3 thin films were determined using this technique and the results are presented in Table 4.2. It is observed that as the temperature increase from 300 to 500℃, the roughness and the particle size of WO_3 also increases (see Table 4.2). Therefore, it can be concluded that the roughness and the particle size of the thin film was affected by the temperature.

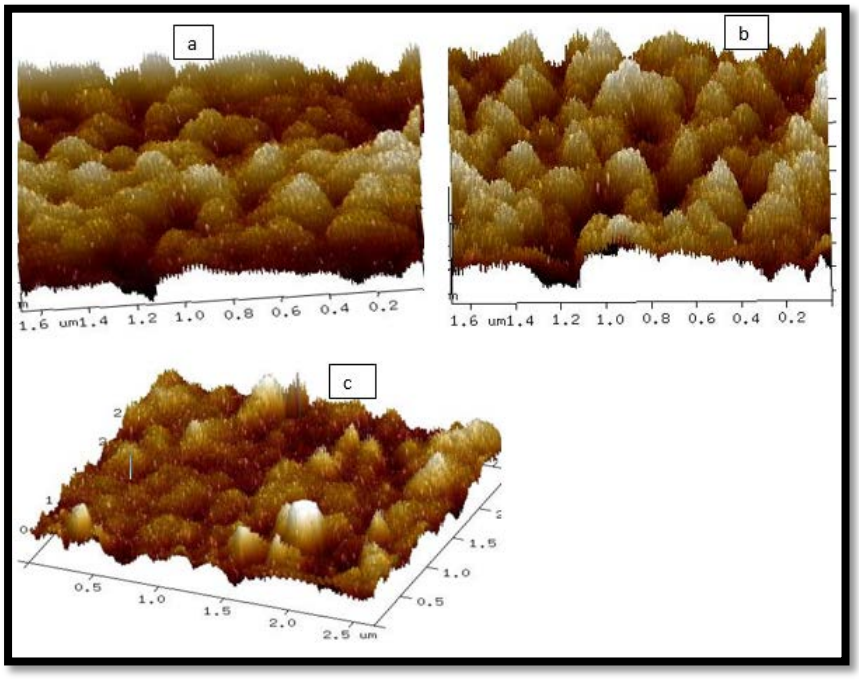

Figure 4.5: The surface topography of the thin film WO_3 nanostructures prepared by DC-magnetron sputtering on silicon substrates at various temperatures (a) 300 ℃, (b) 400 ℃ and (b) 500 ℃.

Table 4-2: The average roughness and particle size distribution of WO_3 prepared at different temperatures

Annealing temperature (°C)	Average roughness (nm)	Particle size distribution (nm)
300	5	16
400	8	19
500	12	35

4.3.4. RBS analyses of WO_3 thin films

The samples were further characterized for composition and thickness using the RBS technique which was carried out using a beam of 3.6 MeV alpha particles ($^4He^{++}$) at iThemba LABS (Gauteng). In Figures: 4.6, 4.7 and 4.8 the RBS spectra are shown. The beam of 3.6 MeV $^4He^{++}$ was incident on a thin film of unknown composition and thickness. It was observed from the RBS as indicated in Table 4.3 that the composition is indeed WO_3. It was also observed from the RBS that the thickness of the samples deposited at different temperatures (300 ºC, 400 ºC and 500 ºC) were not the same. The thickness seemed to increase with an increase in the deposition temperature. The sample deposited at 300 ºC was found to have a thickness of 120 nm, the sample deposited at 400 ºC was found to have a much larger thickness of 360 nm. However, when compared with the sample deposited at 500 ºC, not much difference in thickness was observed

since this sample was found to have a thickness of 370 nm. This increase in thickness might perhaps be attributed to the increase in grain size, structural and phase transformation and particle size of the samples as was observed from the respective results of the XRD and AFM analyses. It should also be noted from the SEM results that the morphology of the samples was not the same, due to the change in deposition temperatures.

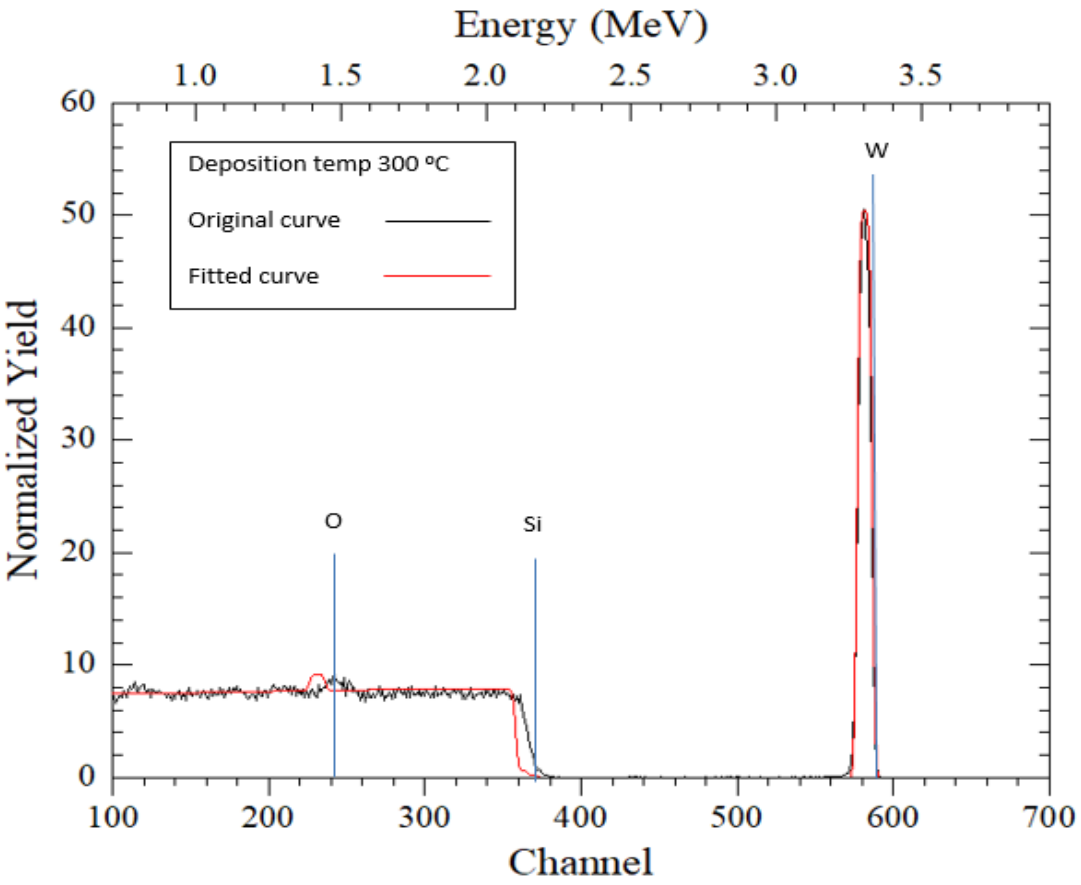

Figure 4.6: RBS spectrum of 3.6 MeV ($4He^{++}$) beam incident on WO_3 thin film deposited at 300°C by DC magnetron sputtering.

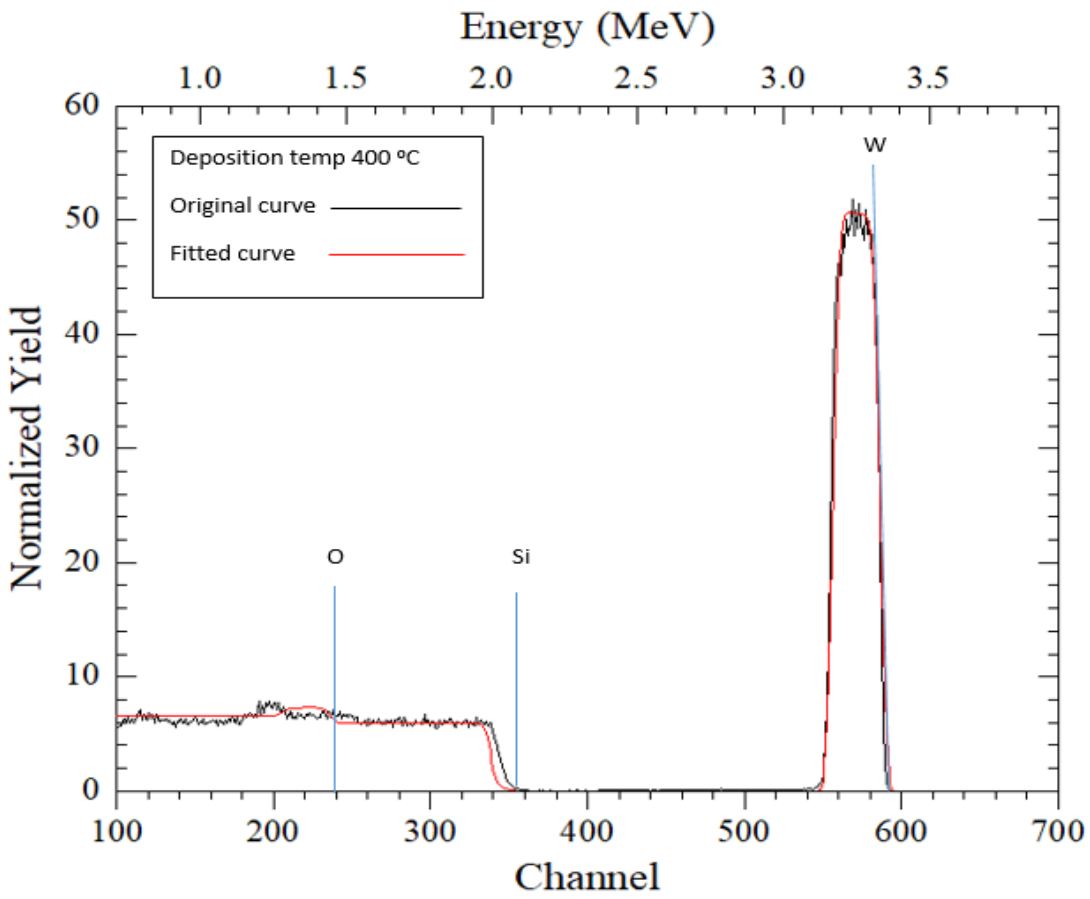

Figure 4.7: RBS spectrum of 3.6 MeV ($4He^{++}$) beam incident on WO_3 thin film deposited at 400ºC by DC magnetron sputtering.

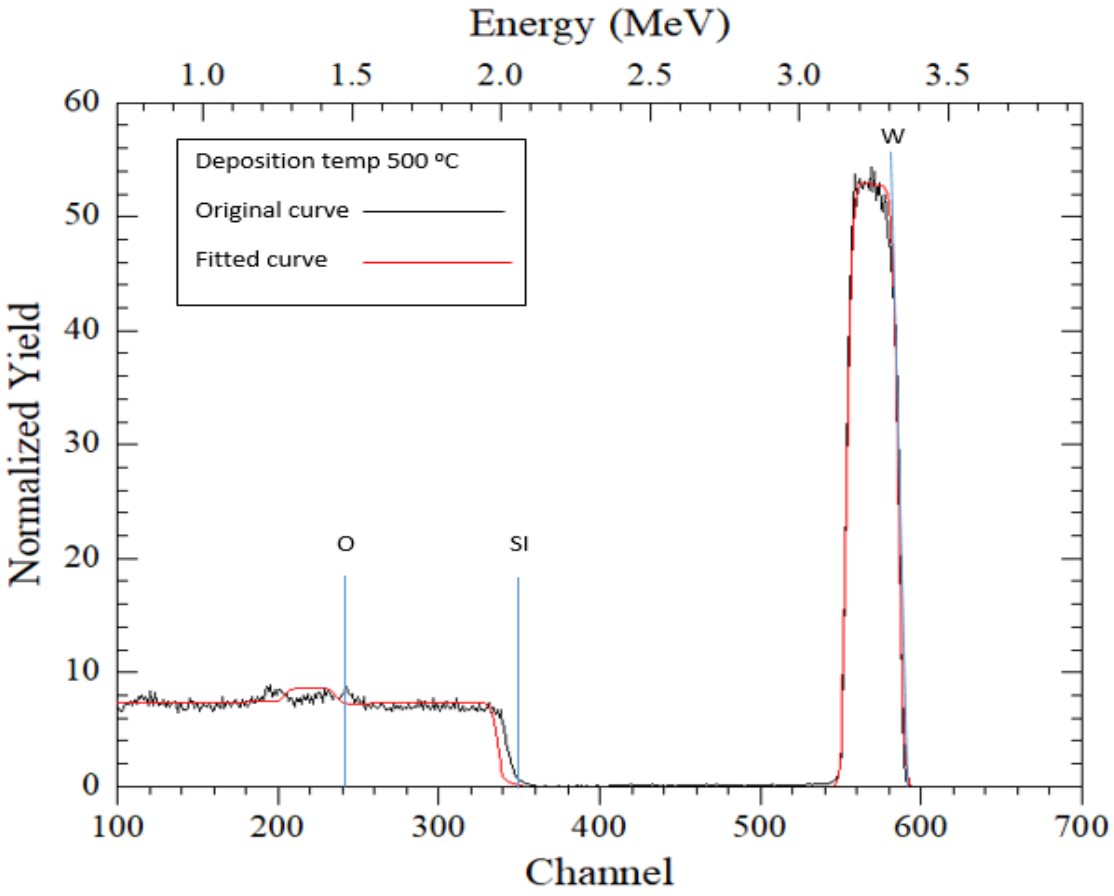

Figure 4.8: RBS spectrum of 3.6 MeV ($4He^{++}$) beam incident on WO_3 thin film deposited at 500 °C by DC magnetron sputtering.

Table 4-3: The composition and thickness of WO_3 prepared at different deposition temperatures

Temperature (°C)	Composition (At%)		Thickness (nm)	Compound
300	W (27%)	O (73%)	120	WO_3
400	W (27%)	O (73%)	360	WO_3
500	W (28%)	O (72%)	370	WO_3

CHAPTER 5:

5. GAS SENSING PROPERTIES OF WO_3 BASED SENSOR FILM

5.1. Introduction: sensor device preparation

WO_3 based sensors were prepared using DC magnetron sputtering at various deposition temperatures (as discussed in detail in Chapter 4) using alumina strip substrates. In Figure 5.1 the schematic diagram of WO_3 based sensor deposited at the alumina substrate is illustrated. The alumina substrate was used because it consists of good electrode/s and its melting point is high (melting point is 1768 ºC) **[10]**. Some previous studies **[18]** have shown WO_3 as a good sensor for NO_2 gas detection. However, in those studies high operating temperatures (250 ºC – 450 ºC) were used during NO_2 detection to try to enhance the sensitivity of the WO_3 based sensor and it has also been reported that WO_3 is not a good sensor at room temperature since it has high activation energy. Therefore, a high operating temperature is required in order to enhance the sensitivity of WO_3 **[47,48]**. High operating temperatures were also used for the ZnO gas sensor to enhance its sensitivity **[49]**. However, a good sensor of NO_2 which will be able to operate at room temperature is also needed since NO_2 may be present at room temperature. In this study we therefore attempt to synthesize a room temperature NO_2 gas sensor based on WO_3. We used a DC magnetron sputtering technique at different deposition temperatures to check if it can improve the sensitivity of the sensor. The WO_3 films were deposited at various temperatures (300, 400, and 500 ºC).

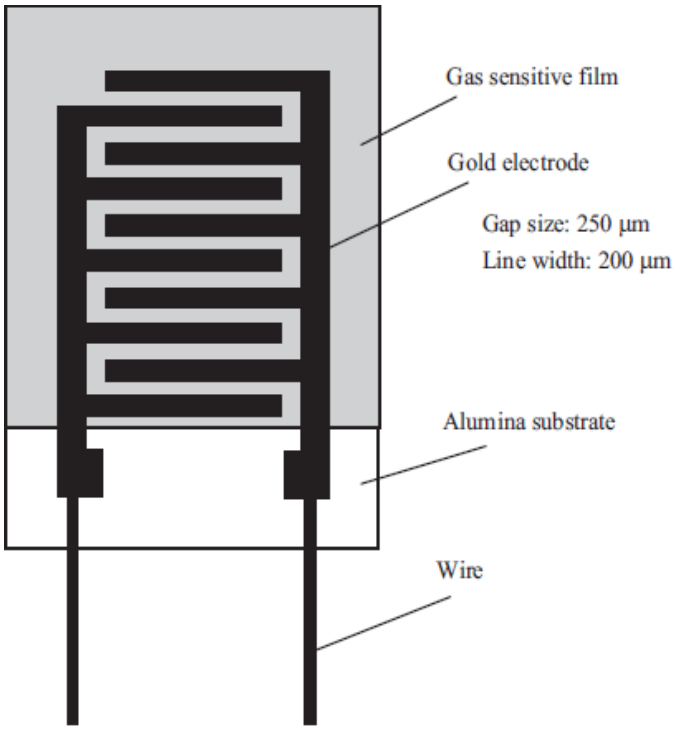

*Figure 5.1: The schematic diagram of a WO_3 based sensor film deposited on an alumina substrate. This diagram was adopted from a previous study **[10]** where gold electrodes were used but in our study an alumina substrate with platinum electrodes was used.*

5.2. Gas sensing characteristics of WO_3 film

WO_3 based sensors which were prepared at different deposition temperatures (300 ºC, 400 ºC and 500 ºC) were each tested for their properties at room temperature in a gas sensing apparatus Kenosistec at the University of Zululand. Before testing the response of the sensors towards NO_2 gas, the sensors were first exposed to different relative humidity (RH%) to check their optimum humidity at room temperature. Figure 5.2 represents the response of the sensors towards 20 ppm NO_2 at room temperature at various relative humidity. It was observed that 70% RH was the optimum humidity for WO_3 based sensors and therefore the gas sensing properties of WO_3 based sensors were tested at 70% RH.

5.3. Relative humidity

It can be noted from Figure 5.2 that the humidity does affect the sensor response of WO_3 as NO_2 gas of 20 ppm is introduced to the surface of WO_3. It can also be seen that from 0% RH to 30% RH the sensor did respond to the incoming NO_2 gas but it did not show even a small recovery. However, the sensor started to show some recovery when the humidity was raised to 70% RH. At 90% RH the sensor did show some recovery. However the response was negatively affected as it seemed to drop when the humidity was above 70% RH. Thus it can be concluded that the optimum humidity for a WO_3 based sensor is 70% RH, since the response and recovery of the sensors for NO_2 gas were good.

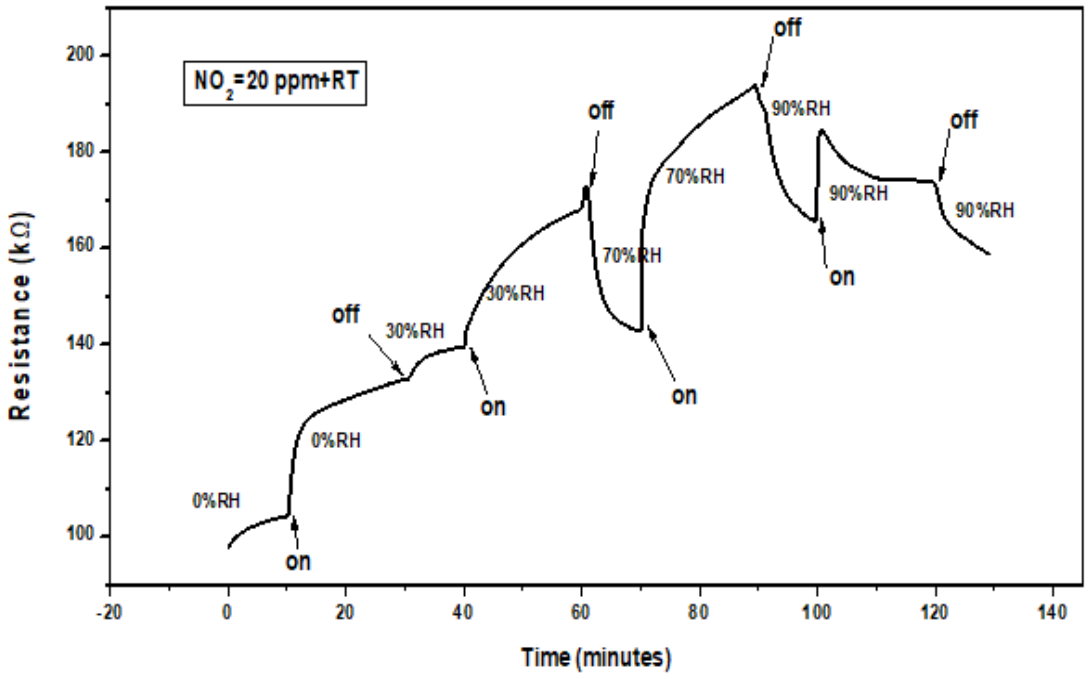

Figure 5.2: The sensor response curve of WO_3 based sensor to 20 ppm concentration of NO_2 gas at room temperature at different relative humidity.

5.4. WO_3 based sensors for NO_2 gas

When a WO_3 based sensor film was exposed to NO_2 gas, the resistance of the sensor increased to a certain value and then decreased to the original resistance once the NO_2 was turned off. This behaviour is normal as reported in previous studies **[10,13,18]** since WO_3 is an n-type metal oxide semiconductor and NO_2 is an oxidising gas. This type of behaviour satisfies R_g/R_a where R_a is the resistance of the sensor, with no gas present on the sensor, and R_g is the resistance of the sensor with gas introduced on the sensor. It shows the chemisorption of NO_2 on the WO_3 surface. Figure 5.3 shows the sensor response curve of the WO_3 metal oxide sensors deposited at 300 ºC, 400 ºC and 500 ºC. These sensors were exposed to different NO_2 concentrations at room temperature and at 70% RH. The NO_2 gas was turned on for 20 minutes to check how fast the sensor was responding to the gas and turned off for 10 minutes to check how fast it was going to recover. It can be seen from Figure 5.3 that the sensors responded immediately to NO_2 gas at all concentrations, but they took some time to recover, and all of them appeared not to be able to recover completely to their original resistance. However, the response and recovery time of the WO_3 based sensor appeared to be slowly improving as the temperature was raised to 500 ºC. This can be clearly seen in Figure 5.5 where response and recovery time of each sensor were calculated.

Figure 5.4 shows the response curve of the WO_3 based sensor deposited at 500 ºC. It can be noted from Figure 5.4 that when the relative humidity was still at 70% RH the response of the sensor was good, but when it was raised to 90% RH during the detection of 150 ppm NO_2, the sensor response behaviour changed. This change shows that the sensor does not perform well at 90% RH. Figure 5.3 and Figure 5.4 show that the initial resistance of WO_3 deposited at 500 ºC changed from an initial value of around 112 kΩ to around 162 kΩ. This was attributed by the fluctuating factors

during gas sensing, e.g. humidity, which was 70% RH±2% RH and the room temperature which was 17.6 ºC± 0.4 ºC.

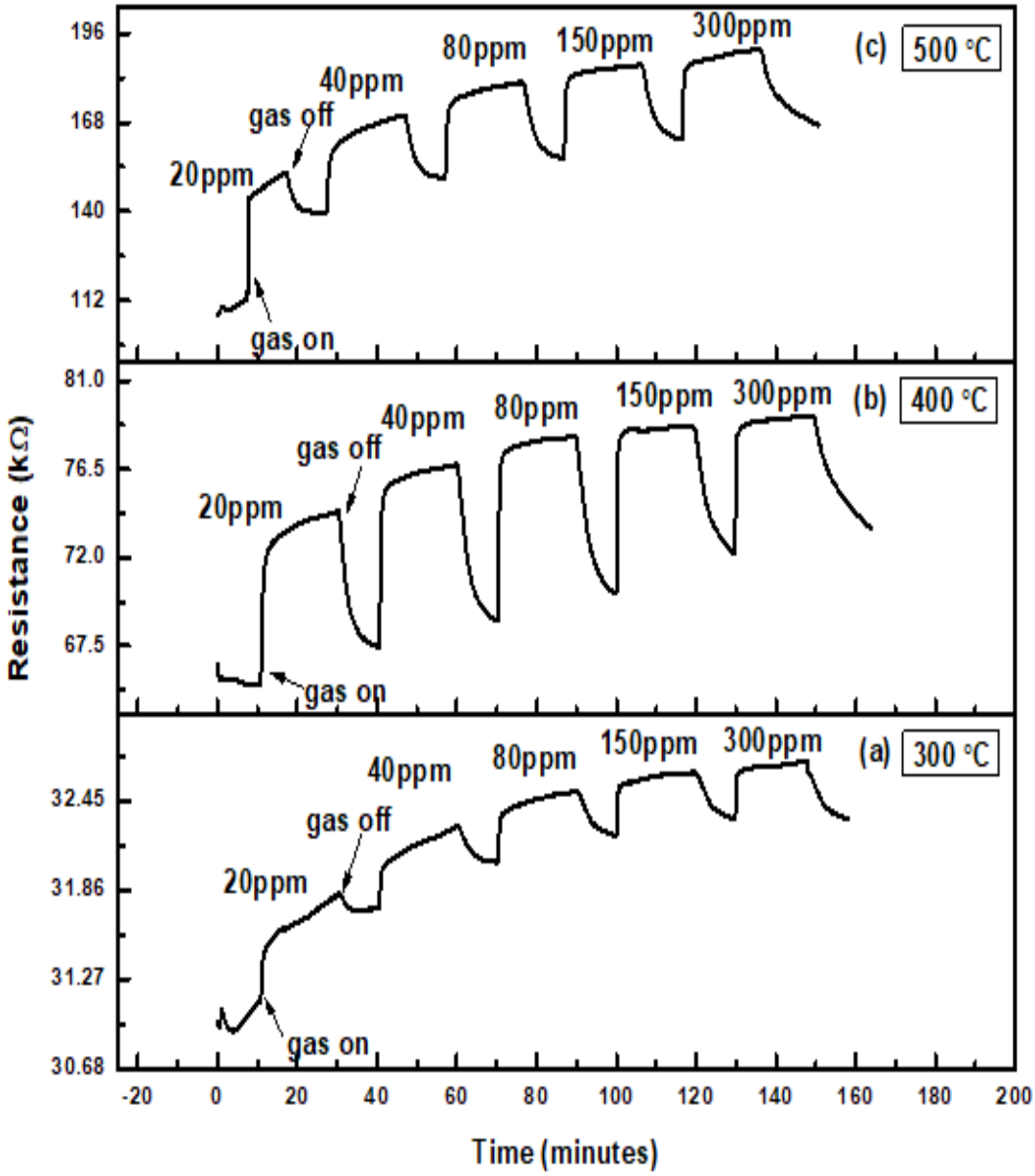

Figure 5.3: WO_3 sensor response curves of the sensors for different NO_2 concentrations. The samples were grown at different deposition temperatures: (a) 300 ºC, (b) 400 ºC, and (c) 500 ºC.

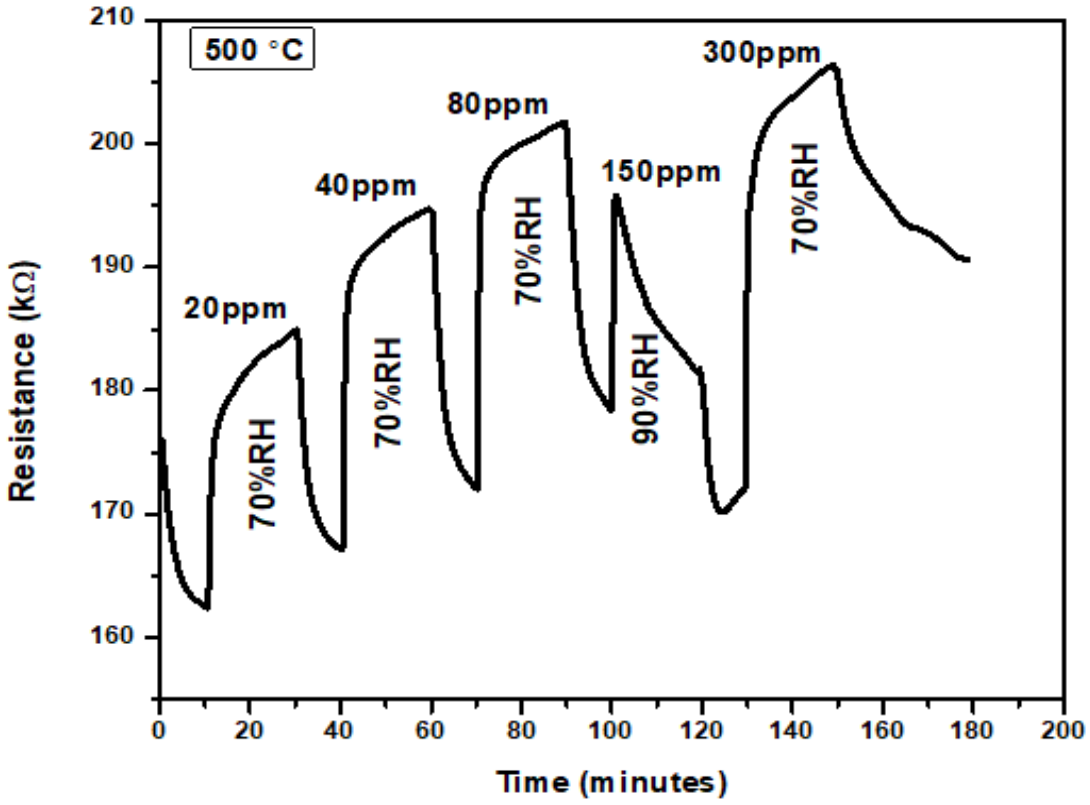

Figure 5.4: The response curve of WO_3 based sensor deposited at 500 ºC showing the effect of increasing humidity to 90%RH.

5.5. Response and recovery time of WO_3 based sensors

The response time and recovery time are of the most important properties of the gas sensors because they reveal how fast the gas sensor respond to that particular target gas and how fast it recovers when the target gas has been turned on and thereafter turned off. This is because the resistance of the sensor changes when it is exposed to the target gas. The change shows that it is able to detect or sense that particular gas **[4-16,50,51]**. In Figure 5.5 the response and recovery time for gas sensors deposited at 300 ºC, 400 ºC and 500 ºC are represented as they were calculated. The sensors were exposed to 80 ppm NO_2 at room temperature and 70% RH. It can be noted from Figure 5.5 that as the temperature increased from 300 ºC to 500 ºC, the response and recovery time

of WO_3 based sensor was improved. It was observed that the response time decreased from 2.37 minutes to 1.80 minutes and the recovery time decreased from 9.81 minutes to 9.43 minutes. Therefore, it can be concluded from Figure 5.5 that the WO_3 based sensor deposited at 500 ºC is a better sensor than those deposited at 300 ºC and 400 ºC. This also agreed to the sensitivity of the three sensors shown in Figure 5.6

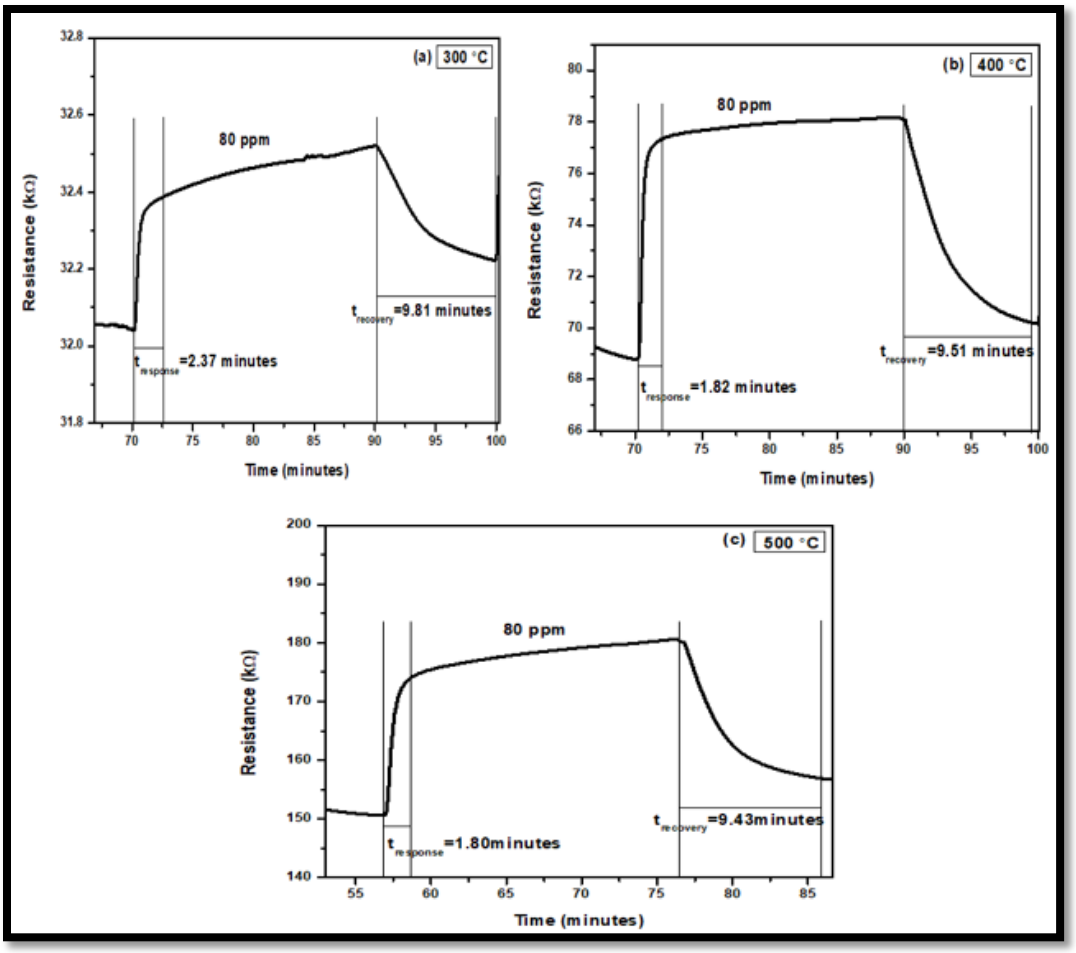

Figure 5.5: The sensor response curves, response and recovery time ($t_{response}$ and $t_{recovery}$) of the sensors to 80 ppm NO_2 at room temperature and 70% RH, deposition temperatures (300 ºC-500 ºC)

5.6. Sensitivity of WO_3 based sensors

The sensitivity is also the most important characteristic of the gas sensor because it tells us the rate at which the gas sensor responds towards the target gas as the concentration of the gas increases **[8-15,52,53]**. The effectiveness of the gas sensor is determined by it sensitivity. The sensitivity ($\Delta S/\Delta C$) is determined from the slope of the linear curve of the sensor response (S) vs concentration (C). In Figure 5.6, the sensor response with concentration of NO_2 gas was plotted for different WO_3 based sensors deposited at different temperatures. It can be noted from Figure 5.6 that the sensitivity of the WO_3 based sensor deposited at 500 ºC is a bit higher than that of the other two sensors deposited at lower temperatures. The sensitivity was calculated from 80 ppm to 150 ppm for all three sensors. This is also true when looking at other concentrations (20 ppm to 40 ppm, 40 ppm to 80 ppm, and 150 ppm to 300 ppm). The sensitivity of WO_3 deposited at 500 ºC for these concentrations is higher than those deposited at 300ºC and 400ºC.

Since the WO_3 based sensor deposited at 500 ºC was the one with better sensitivity, it was further tested to varying NH_3 gas concentrations and also to hydrogen gas at the same sensing environment (room temperature and 70% RH). It can be observed from Figure 5.7 that the WO_3 based sensor was able to respond to NH_3 gas. However, the behaviour of this sensing was not clear and the response to this gas was not good compared to the response to NO_2. In Figure 5.8 it can be observed also that WO_3 was not able to detect hydrogen gas even though the hydrogen concentrations were varied. This was perhaps because NH_3 and H_2 are both reducing gases.

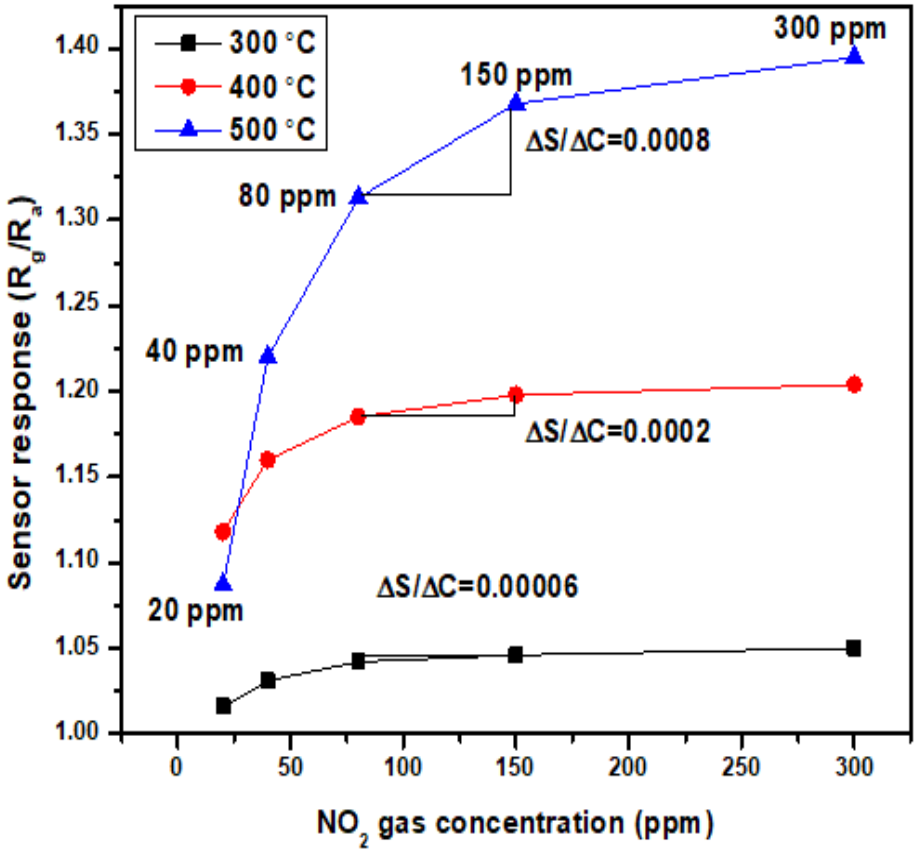

Figure 5.6: The comparison of sensor response values and sensitivity of WO_3 based sensors of different deposition temperatures.

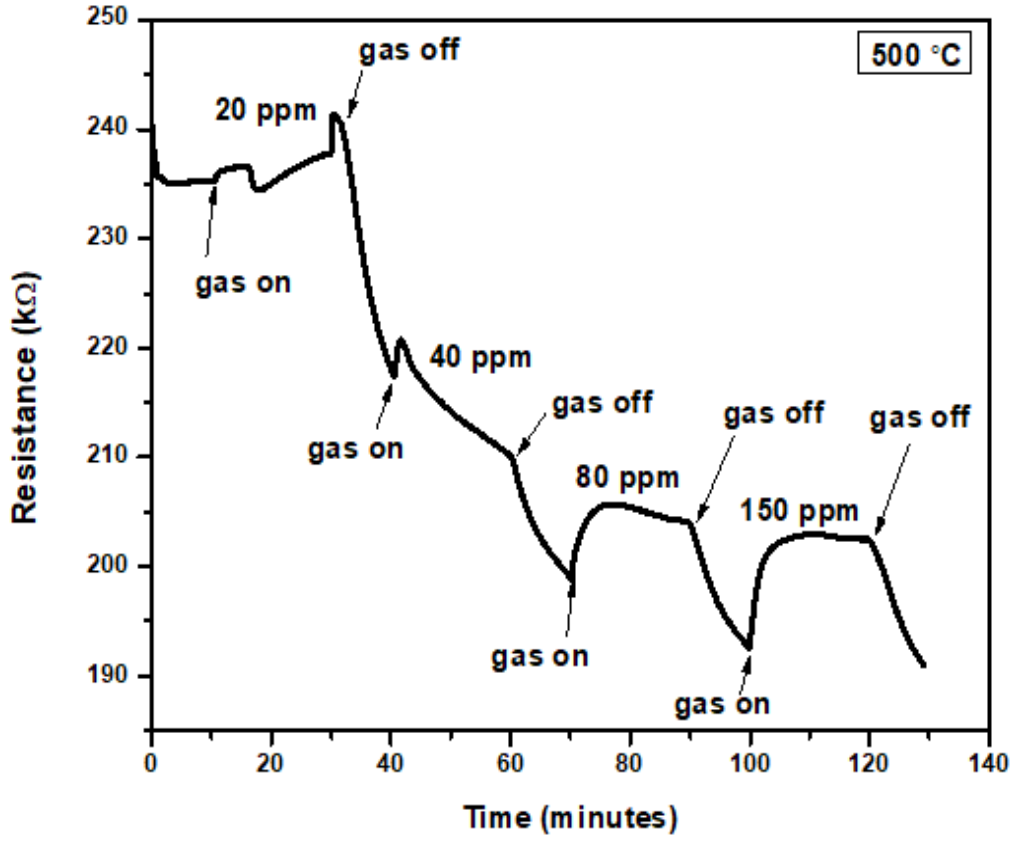

Figure 5.7: The sensor response curve of a WO_3 based sensor deposited at 500 ºC to the varying NH_3 concentrations.

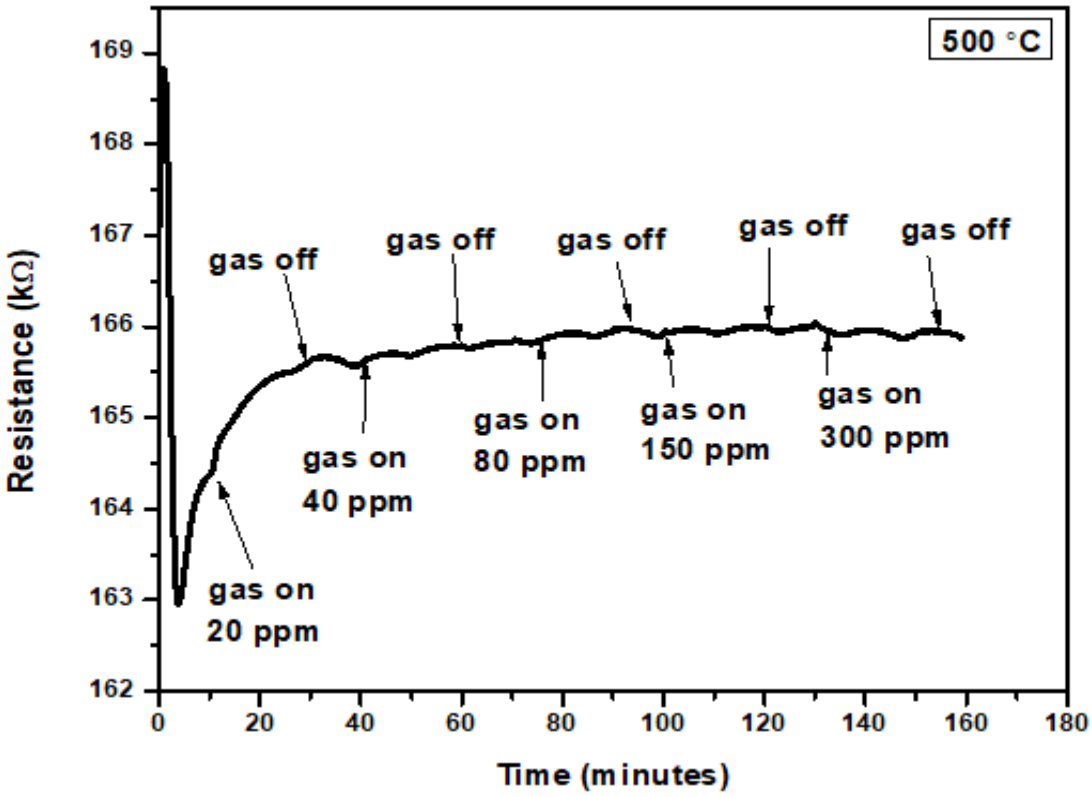

Figure 5.8: The sensor response curve of a WO_3 based sensor deposited at 500 ºC to the varying H_2 concentrations.

C. Zhang et al.**[23]** has reported a good sensing response of WO_3 towards different concentrations of H_2, this disagree with the results of the present study since no detection of H_2 gas was observed. The possible reasons for this disagreement is that in C. Zhang et al.**[23]** study, it was reported that WO_3 synthesized was monoclinic in crystal structure, however in the present study WO_3 obtained was amorphous, hexagonal and tetragonal in structure. It was noted from the previous studies that WO_3 nanostructures with different morphological structures and crystal structures can be fabricated or synthesized when different methods and techniques to synthesize WO_3 are used,

therefore the variation of WO_3 nanostructures in morphology and crystal structure results in WO_3 to have different gas sensing properties **[3,10,11,13,21,23]**.

5.7. Conclusion

The three WO_3 based sensors of different deposition temperatures (300, 400 and 500 ºC) were tested for their gas sensing properties. The effect of humidity was first investigated by exposing them to 20 ppm of NO_2 while varying humidity at room temperature and it was found that 70% RH is the optimum humidity to detect gases, as shown in Figure 5.2. Figure 5.4 proves that the humidity plays a critical role during the gas sensing of the target gas as it was observed that at 90% RH the sensor response was affected negatively to 150 ppm of NO_2. The response time and recovery time of the WO_3 based sensor deposited at 500 ºC proved that this sensor is better than those deposited at 300 ºC and 400 ºC since its response and recovery times were fast, and the same thing applied to the sensitivity, therefore the good sensitivity was observed for WO_3 which is tetragonal in structure. The increase in roughness (from AFM results) of WO_3 film has resulted to the increase of sensing performance of WO_3 gas sensor. The tetragonal phase of WO_3 showed a great improvements of sensor response towards NO_2 gas compared to the amorphous and hexagonal phases. When this sensor was exposed to NH_3 and H_2 gas it did not respond well to these gases. This is probably because these are reducing gases.

CHAPTER 6

6. SUMMARY AND CONCLUSION

WO_3 thin films were successfully deposited on silicon (111) and alumina strips substrates using DC magnetron sputtering at different deposition temperature (300, 400 and 500 ºC). WO_3 thin films were characterized using XRD, SEM equipped with EDS, AFM and RBS. From the XRD studies it was found that the samples (WO_3 thin films) were different in crystal structures due to the phase transformation as the deposition temperature increases. Amorphous WO_3 was observed at 300 ºC, polycrystalline WO_3 of hexagonal and tetragonal structures were observed at 400 ºC and 500 ºC respectively. An increase in grain size of the samples with an increase in deposition temperature was also observed. From the SEM work it was also found that the deposition temperature has an effect on the sample morphology since the morphologies of the samples were completely different from each other. From the AFM measurements it was also found that the sample roughness and particle size distribution increased with an increase in deposition temperature. RBS confirmed that thin films of WO_3 deposited on silicon (111) and alumina strip substrates were stoichiometric, and that increasing the deposition temperatures increased the thickness of the samples. This was attributed to the increase in grain sizes and particle sizes of the samples. This was confirmed by both the XRD and AFM measurements.

The samples were further tested on a gas sensing apparatus (Kenosistec) for their gas sensing performance at room temperature. It was found that the sample deposited at 500 ºC had a better gas sensing performance than those that were deposited at 300 ºC and 400 ºC, and that it could be effectively used to sense NO_2 gas at room temperatures under the humidity of 70% RH. This NO_2 gas sensor based on the WO_3 film deposited at 500 ºC exhibited the n-type behaviour of sensing

since the exposure to NO_2 gas resulted in the increase in its resistance. This is a normal behaviour since NO_2 is an oxidising gas and WO_3 is an n-type metal oxide.

Future work

Future work will focus on WO_3 doped with CNTs/CNS and other p-type semiconductors to check how much improvement can be achieved to the WO_3 sensitivity.

References

[1] T.V. Duncan. *Applications of nanotechnology in food packaging and food safety: Barrier materials, antimicrobials and sensors*. Journal of Colloid and interface Science 363 (2011) 1-24.

[2] A.I. Lopez-Lorente, M. Valcarcel. *The third way in analytical nanoscience and nanotechnology: Involvement of nanotools and nanoanalytes in the same analytical process*. Trends in Analytical Chemistry 75 (2016) 1-9.

[3] W. Zhang, M. Hu, X. Liu, Y. Wei, N. Li, Y. Qin. *Synthesis of the cactus-like silicon nanowires/tungsten oxide nanowires composite for room-temperature NO2 gas sensor*. Journal of Alloy and Compounds 679 (2016) 391-399.

[4] H. Zheng, J.Z. Ou, M.S. Strano, R.B. Kaner, A. Mitchell, K. Kalantar-zadeh. *Nanostructured tungsten oxide-properties, synthesis, and applications*. Adv. Funct. Mater. 21 (2011) 2175.

[5] S.K. Chong, C.F. Dee, S.A. Rahman. *Single reactor deposition of silicon/tungsten oxide core-shell heterostructure nanowires with controllable structure and optical properties*. RSC Adv. 5 (2015) 2346-2353.

[6] N. Lavanya, A.C. Anithaa, C. Sekar, K. Asokan, A. Bonavita, N. Donato, S.G. Leonardi, G. Neri. *Effect of gamma irradiation on structural, electrical and gas sensing properties of tungsten oxide nanoparticles*. Journal of Alloys and Compounds 693 (2017) 366-372.

[7] E. Lassner, Wolf. Schubert (1999). *Tungsten: properties, chemistry, technology of the element, alloys and chemical compound*. New York: Kluwer Academic. ISBN 0-306-45053-4.

[8] S. Goutham, S. Kaur, K.K. Sadasivuni, J.K. Bal, N. Jayarambabu, D.S. Kumar, K.V. Rao. *Nanostructured ZnO gas sensors obtained by green method and combustion technique*. Materials Science in Semiconductor Processing 57 (2017) 110-115.

[9] G. Sun, H. Kheel, J.K. Lee, S. Choi, S. Lee, C. Lee. *H2S gas sensing properties of Fe2O3 nanoparticle-decorated NiO nanoplate sensors*. Surface and Coatings Technology 307 (2016) 1088-1095.

[10] P.G. Su, T.T. Pan. *Fabrication of a room-temperature NO2 gas sensor based on WO3 films and WO3/MWCNT nanocomposite films by combining polyol process with metalorganic decomposition method*. Materials Chemistry and Physics 125 (2011) 351–357.

[11] S. Haviar, S. Chlupova, P. Kus, M. Gillet, V. Matolin, I. Matolinova. *Micro-contacted self-assembled tungsten oxide nanorods for hydrogen gas sensing*. International Journal of Hydrogen Energy 42 (2016) 1-9.

[12] S.B. Upadhyay, R.K. Mishra, P.P. Sahay. *Cr-doped WO3 nanosheets: Structural, optical and formaldehyde sensing properties*. Ceramics International 42 (2016) 15301-15310.

[13] E. Ciftyurek, K. Sabolsky, E.M. Sabolsky. *Molybdenum and tungsten oxide based gas sensors for high temperature detection of environmentally hazardous sulfur species*. Sensors and Actuators B237 (2016) 262-274.

[14] T. Vilic, E. Llobet. *Nickel doped WO3 nanoneedles deposited by a single step AACVD for gas sensing applications*. Procedia Engineering 168 (2016) 206-210.

[15] M.H. Chen, Z.C. Huang, G.T. Wu, G.M. Zhu, J.K. You, Z.G. Lin. *Synthesis and characterization of SnO-Carbon nanotube composite as anode material for lithium-ion batteries*. Mater. Res. Bull. 38 (2003) 831-836.

[16] V.H. Nguyen, A.P.D. Nguyen, T. Tran, A.T. Mai, D.C. Nguyen. *Gas-sensing properties of tin oxide doped with metal oxides and carbon nanotubes: A competitive sensor for ethanol and liquid petroleum gas*. Sensors and Actuators B144 (2016) 450-456.

[17] W. Wang, P. Serp, P. Kalck, J.L. Faria. *Photocatalytic degradation of phenol on MWCNT and titania composite catalysis prepared by a modified sol-gel method*. App. Catal. B: Environ. 56 (2004) 301-308.

[18] B. Urasinska-Wojcik, T.A. Vincent, M.F. Chowdhury, J.W. Gardner. *Ultrasensitive WO3 gas sensors for NO2 detection in air and low oxygen environment*. Sensors and Actuators B 239 (2017) 1051-1059.

[19] A.S. Alshammari, M.R. Alenezi, K.T. Lai, S.R.P. Silva. *Inkjet printing of polymer functionalized CNT gas sensor with enhanced sensing properties*. Materials Letter 189 (2017) 299-302.

[20] A. Kumar, S. Keshri, D. Kabiraj. *Influence of annealing temperature on nanostructured thin films of tungsten trioxide.* Materials Science in Semiconductor Processing 17 (2014) 43–52.

[21] Y. Wei, M. Hu, W. Yan, D. Wang, L. Yuan, Y. Qin. *Hydrothermal synthesis porous silicon/tungsten oxide nanorods composites and their gas-sensing properties to NO2 at room temperature.* Applied Surface Science 353 (2015) 79-86.

[22] D.R. Miller, S.A. Akbar, P.A. Morris. *Nanoscale metal oxide-based heterojunctions for gas sensing: A review.* Sensors and Actuators B 204 (2014) 250-272.

[23] C. Zhang, A. Boudiba, M.G. Olivier, R. Snyders, M. Debliquy. *Magnetron sputtered tungsten oxide films activated by dip-coated platinum for ppm-level hydrogen detection.* Thin Solid Films 520 (2012) 3679-3683.

[24] X. Chia, C. Liub, L. Liua, Y. Lia, Z. Wanga, X. Boa, L. Liua, C. Su. *Tungsten trioxide nanotubes with high sensitive and selective properties to acetone.* Sensors and Actuators B 194 (2014) 33– 37.

[25] D. Valerini, S. Hernández, F. DiBenedetto, N. Russo, G. Saracco, A. Rizzo. *Sputtered WO3 films for water splitting applications.* Materials Science in Semiconductor Processing 42 (2016) 150-154.

[26] D. Valerini, S. Hernández, F. DiBenedetto, N. Russo, G. Saracco, A. Rizzo. *Sputtered WO3 films for water splitting applications.* Materials Science in Semiconductor Processing 42 (2016) 150-154.

[27] T.G. Nyawo. *Reactive magnetron deposition and characterization of ZrN thin films for decorative and field emission applications.* MSc thesis. UniZulu (2012) 1-99.

[28] E. Alfonso, J. Olaya, G. Cubillos. *Thin Film Growth Through Sputtering Technique and Its Applications*. Universidad Nacional de Colombia. 397-429.

[29] Z.Y. Nuru, C.J. Arendse, T.F.G. Muller, S. Khamlich, M. Maaza. *Thermal stability of electron beam evaporated AlxOy/Pt/AlxOy multilayer solar absorber coatings*. Solar energy materials & solar cells 120 (2014) 473 – 480.

[30] K. Seshan. *Handbook of thin-film deposition processes and techniques*. (2002) 1-607.

[31] D. Depla, S. Mahieu, J.E. Greene. *Sputter deposition processes*. (2010) 1-36.

[32] N.S. Chonco. *Synthesis and characterisation of DLC and diamond films for gas sensing applications*. MSc thesis. Unizulu (2014) 1-96.

[33] [www 1] http://www.amse.org.cn/article/2014/1006-7191-27-2-324/40195_2014_48_Fig1_HTML.gif (20/03/2014).

[34] [www 2] https://www.chem.uci.edu/~lawm/263 4.pdf (20/03/2017).

[35] [www 3] http://serc.carleton.edu/research_education/geochemsheets/techniques/XRD.html (25/03/2017).

[36] [www 4] http://www.columbia.edu/itc/hs/dental/sophs/material/production_xrays.pdf (27/03/2017).

[37] Y. Watanabe. *Production of X-rays*. Masonic cancer center M10-M (2016) 1-32.

[38] [www 5] http://nau.edu/uploadedImages/Academic/CEFNS/Labs/Electron_Microprobe/_Media/Bremsstrahlung.jpg (02/04/2017).

[39] B. Cheney. Introduction to Scanning Electron Microscopy. Materials Engineering department San Jose State (2007) 2-12.

[40] [www 6] http://www.purdue.edu/ehps/rem/rs/sem.htm (03/04/2017).

[41] [www 7] http://cdn.iopscience.com/images/0957-4484/25/18/185705/Full/nano490588f2_online.jpg (03/04/2017).

[42] [www 8] http://www.keysight.com/main/editorial.jspx?ckey=1774141&id=1774141&nid=-33986.0&lc=spa&cc=VE, (09/04/2017).

[43] E. Meyer. *Atomic force microscopy. Progress in Surface Science*. Vol.41 (1992) 3-49.

[44] M. Mayer. *Rutherford Backscattering Spectrometry (RBS)*. Lectures given at the Workshop on Nuclear Data for Science and Technology: Materials Analysis Trieste, 19-30 May 2003.

[45] [www 9] minerva.union.edu/labrakes/RBS%20Physics%20300%20S07.ppt (04/05/2017).

[46] [www 10] http://www.caiciss.co.uk/kinematic.pdf (04/05/2017).

[47] Y.G. Choi, G. Sakai, K. Shimanoe, N. Miura, N. Yamazoe, Sens. *Receptor Function and Response of Semiconductor Gas Sensor*. Actuators B 95 (2003) 258–265.

[48] T. Kida, A. Nishiyama, M. Yuasa, K. Shimanoe, N. Yamazoe. *Metal Oxide Semi-Conductor Gas Sensors in Environmental Monitoring*. Sens. Actuators B 135 (2009) 568–574.

[49] J.F. Chang, H.H. Kuo, I.C. Leu, M.H. Hon. *The effects of thickness and operation temperature on ZnO:Al thin film CO gas sensor*. Sensors and Actuators B 84 (2002) 258–264.

[50] U. Yaqoob, D.T. Phan, A.S.M.I. Uddin, G.S. Chung. *Highly flexible room temperature NO2sensor based onMWCNTs-WO3nanoparticles hybrid on a PET substrate*. Sensors and Actuators B 221 (2015) 760–768.

[51] S. Keshtkar, A. Rashidib, M. Kooti. *Development of tin dioxide quantum dots/multi-walled carbon nanotubes and tin dioxide quantum dots/carbon nanohorns nanohybrids as low temperatures natural gas sensors*. Ceramics International 43 (2017) 14326–14333.

[52] D. Zhang, Z. Wu, P. Li, X. Zong, G. Dong, Y. Zhang. *Facile fabrication of polyaniline/multi-walled carbonnanotubes/molybdenum disulfide ternary nanocomposite and its high-performance ammonia-sensing at room temperature*. Sensors and Actuators B 258 (2018) 895–905.

[53] Y. Li, D. Deng, N. Chen, X. Xing, X. Liu, X. Xiao, Y. Wang. *Pd nanoparticles composited SnO2 microspheres as sensing materials for gas sensors with enhanced hydrogen response performances*. Journal of Alloys and Compounds 710 (2017) 216-224.